



How to Extract Lagrangian Information from Cloud Radar Doppler Spectra for Process Studies?

Paul Ockenfuß¹, Gregor Köcher¹, Isabel Petit¹, and Stefan Kneifel¹

¹Meteorologisches Institut, Ludwig-Maximilians-Universität München, München, Germany

Correspondence: Paul Ockenfuß (paul.ockenfuss@physik.uni-muenchen.de)

Abstract. Ground-based remote sensing instruments are often operated in a vertically pointing mode, producing time-height cross-section images (THIs) of the atmosphere. However, THIs are not Lagrangian observations: they cannot track the evolution of a single particle directly. Instead, several assumptions are required to derive the particle evolution from THI. We discuss these assumptions and show how their validity can be assessed using elevation scans. For demonstration, we analyze two intense riming cases. Since rimed particles exhibit enhanced sedimentation velocities, we first present a method to derive the vertical target velocity from scanning cloud radar observations. This method allows to study the spatial distribution of riming. The first case is comprised of several horizontally homogeneous, descending layers of rimed particles. Under these conditions, one can safely study the particle evolution in a "traditional" way by evaluating subsequent vertical profiles. The second case is more heterogeneous. For the analysis, we introduce the new spectral column vertical profile (SCVP) technique. SCVPs allow to trace the evolution of a single particle population's Doppler spectrum in space and time, thereby representing true Lagrangian observations. Our results demonstrate the value of scanning observations and show that downsides, for example regarding the use of Doppler velocity, can be overcome. Our results also raise the question whether the typically very high time resolution of THI is actually required for the common type of analyses performed on THI, and whether a combination of scanning and vertical observations could be the better observational strategy for ground-based remote sensing instruments.

1 Introduction

Clouds and the underlying microphysical processes have a huge influence on the Earth system, for example through cloud radiative fluxes and feedbacks (e.g. Andrews et al., 2012) or the global water cycle (e.g. Heymsfield et al., 2020). In order to improve the understanding of clouds, there was substantial progress in the development and adoption of Lagrangian cloud models in the recent years (Grabowski et al., 2019). Those models track the evolution of single (super-)particles in space and time. Lagrangian models have been successfully applied to simulate warm rain processes (e.g. Lim and Hoffmann, 2024) and the ice phase (e.g. Brdar and Seifert, 2018). Nevertheless, many of the underlying processes governing the particle evolution, especially in the ice phase, are still poorly understood (Morrison et al., 2020). This can partly be attributed to the inability of many observational techniques to observe process rates in a Lagrangian sense. As recently discussed by Feingold et al. (2025), airborne and satellite observations essentially provide contiguous "snapshots" in time of the cloud system. From Feingold et al. (2025): "Neither approach tracks a parcel of air in time, a view that would yield more direct insights into the evolving



system." In contrast to flying platforms, ground based instruments like radars often operate in a vertically pointing mode. In this configuration, they record vertical profiles that are typically displayed as time-height images (THIs). Even though THIs provide continuous observations from a single location, they do not provide continuous observations of a single particle. As we are going to illustrate in section 2, THIs represent a mixture of the spatial variability and temporal evolution of the scene.

30 In this work, we are going to study the assumptions, which are necessary to derive process rates from THIs. We will show how radar scans can be used to assess the validity of these assumptions and how they can allow for process studies even in conditions where THIs can not be used anymore.

To this end, we will start by revisiting what we see in THIs and how the appearing characteristic structures, especially fall streaks, are formed. Using three idealized examples, we will illustrate the ambiguity when interpreting the shape of fall streaks, as well as the measurements along a fall streak. Marshall (1953) already pointed out that rapidly scanning radars performing elevation scans—now commonly referred to as range-height indicator (RHI) scans— can provide a more complete view of the atmospheric scene to resolve these ambiguities. More recently, this idea was brought to life by Kollias et al. (2014a), who presented several RHI scanning strategies that reveal the actual three-dimensional structure of clouds. By combining multiple successive scans, their approach can be leveraged into a four dimensional lagrangian analysis. Borque et al. (2014) demonstrated this by using along-wind RHI (AWRHI) scans for the Lagrangian tracking of shallow cumuli in space and time. However, their analysis focused exclusively on the evolution of radar reflectivity.

35
40

In addition to reflectivity, nearly all cloud radars measure the radial velocity of hydrometeors, either as the mean Doppler velocity (MDV) within the sampling volume or as a full Doppler spectrum. In the latter case, the individual contributions of scatterers with different velocities to the total reflectivity are retained. In THI, Doppler spectra are known to provide a versatile source of information on cloud microphysics (e.g. Shupe et al., 2004). In slanted observations, however, Doppler information remains rarely used, because horizontal wind strongly influences the measured radial velocity. Most studies that use MDV in scanning configurations do so to retrieve the horizontal wind field, as in Kollias et al. (2014b). A rare example of exploiting slanted Doppler spectra is given by Hajipour et al. (2025). Their focus, however, was not on spatial structure or temporal evolution; instead, they assumed horizontal homogeneity and investigated the angular dependence of polarimetric variables.

45
50 In section 3, we introduce methods to retrieve sedimentation speed from slanted beams and therefore make Doppler spectra usable for scans and Lagrangian analysis.

For demonstration, we will focus on two pronounced riming events. Riming, i.e., the collision and subsequent freezing of supercooled liquid water droplets onto falling ice crystals, is a key precipitation-generating process in mixed-phase clouds (Borys et al., 2000; Korolev et al., 2017; Morrison et al., 2020). Ground-based observations indicate that more than 50 % of the surface snow mass can consist of rime ice (Mitchell et al., 1990; Borys et al., 2003; Zhang et al., 2021), and modeling studies have shown that riming efficiency significantly affects precipitation accumulation (Seifert et al., 2019; DeLaFrance et al., 2024). Nevertheless, observing riming within clouds remains challenging. Radar reflectivity signatures of riming are difficult to distinguish from those of aggregation, as both processes increase reflectivity. Similarly, the polarimetric signature of riming is ambiguous because particles become both denser and rounder (Kumjian et al., 2022).

55



60 One of the few robust methods for detecting riming relies on measuring particle fall speeds with vertically pointing Doppler radar. In THIs, riming typically appears as characteristic, often striped regions of enhanced fall velocity in the sub-zero part of the cloud. Kneifel and Moisseev (2020) showed that for fall speeds exceeding 1.5 m s^{-1} , particles are very likely to consist of more than 50 % rime ice. Building on this criterion, Ockenfuß et al. (2025) identified riming events in non-convective clouds and compiled comprehensive statistics. From the duration of these events, they inferred that the spatial extent of riming regions
65 can reach several tens of kilometers. However, because their analysis relied solely on THI, they could not directly observe the three-dimensional structure of these regions or verify the underlying advection assumption.

With our new method, we will analyze two riming cases, showing that the first case is rather homogeneous and therefore allows for traditional THI analysis. The second case is inhomogeneous and requires a different approach. Therefore, we introduce a new diagnostic in analogy to column vertical profiles (CVP; Murphy et al., 2020), which we call spectral CVP (SCVP).
70 These are spectrograms, constructed from multiple beams along a single virtual transect through the domain. They will allow us to follow a specific particle population over several minutes in a truly Lagrangian sense. This is, to our knowledge, the first study that makes use of radar as a "five dimensional tool", combining space, time and spectral dimension into a consistent picture.

The manuscript is structured as follows. We begin with the recap of fall streaks in THI in section 2. We then introduce the
75 measurement strategy employed in this study and the theoretical framework, which we developed to process slanted Doppler measurements in section 3. In section 4, we present the two case studies. For each case, we first analyze the observations from the perspective of the THI, then evaluate the scanning measurements, and finally investigate their temporal and spatial evolution. In subsection 5.1, we discuss our findings with respect to insights into the riming process. Subsection 5.2 is dedicated to the discussion of the assumptions and potential side effects of our processing method. In section 6, we point out what our
80 results imply for operational cloud radar scanning strategies and we give suggestions for future measurement campaigns.

2 On the interpretation of fall streaks

To provide a foundation for the subsequent analysis, we first recapitulate what THI represent and how fall streaks form. Thereby, we extend the discussions provided in e.g. Marshall (1953) and Hogan and Kew (2005). We simulate three idealized scenarios in which particles are generated at a height of 3 km, fall downward with constant vertical velocity, and are advected
85 by a horizontally varying wind field. The horizontal wind blows steadily from right to left and exhibits vertical shear. We compute particle trajectories by solving the kinematic equation of motion ($\dot{\mathbf{x}} = \mathbf{v}_{\mathbf{x}}$), using a fourth-order Runge-Kutta integration scheme.

In the first column of Figure 1, we show a spatial snapshot of particle positions at a fixed time. Each particle has a number for easier identification and carries a measurable property, indicated by the color. In reality, the property may be any measurable
90 quantity of interest, for example the radar reflectivity. The radar is located at $x = 15 \text{ km}$ at the surface and points vertically upward. In the second column, we display the corresponding radar measurement as a THI. The third column gives information



about the wind field and sedimentation velocity. At this point, the reader is also referred to the animations provided with the publication.

Scenario A (first row) depicts a localized, continuously seeding cell that moves with the background wind. This configuration
95 corresponds to the conceptual model discussed by Marshall (1953). The particles are always generated with a property value
of 0, which then increases continuously while falling down (this is easier to see in the animation). As evident in Figure 1a,
the fall stripe—that is, the spatial pattern formed by the ensemble of particles—differs from the individual particle trajectories
(indicated by dashed lines). For constant sedimentation velocity and linear wind shear, Marshall (1953) showed that the fall
streak has a parabolic shape both in physical space and in the corresponding THI (Figure 1b). As we can see, the evolution of
100 the particle property (colors) along the fall streak provides a realistic representation of the actual, lagrangian evolution of each
single particle.

However, the mere presence of a fall streak in a THI does not imply the existence of a continuously generating cell. Scenario B (second row) demonstrates the converse situation: a spatially extended but instantaneous seeding event that produces a layer of descending particles. Similar to Scenario A, this configuration also yields a continuous fall streak in the THI, although
105 in this case the shape is linear, rather than parabolic. In reality, the exact shape of fall streaks varies due to changes in wind
shear, particle fall velocity, and turbulence. As in Scenario A, the variation of the particle property along the fall streak is a
representation of the particle evolution.

As is evident, different spatial scenarios can lead to the formation of a fall streak in a THI. The only immediate conclusion
that can be drawn from the presence of a fall streak is that the underlying seeding event must be extended either in space or in
110 time. If the particle generation is neither spatially nor temporally extended—i.e., if it is both short-lived and localized—we do
not observe a fall streak spanning the full vertical extent, as illustrated in Scenario C (third row).

In Scenario C, particles are generated at one instant in time in a localized area. This leads to the formation of a short fall
streak in Figure 1h, which "disappears" in midair. In Scenario C, the analysis of the fall streak would again indicate a temporal
evolution of the particle property. However, this is not the case. As is visible in the corresponding animation, the particles
115 undergo no evolution. Instead, their generation is heterogeneous: their property depends on the location of formation.

These examples highlight a fundamental limitation of THIs: each particle is sampled exactly once as it passes through the
radar beam. When we track fall streaks to infer particle evolution and process rates, we need to assume spatial homogeneity:
Particles formed at different positions must have the same initial properties and must undergo the same evolution. Only under
this condition, we can interpret a series of observations of different particles as representative for the evolution of each single
120 particle. Alternatively, it is also possible to retrieve spatial variability from THI variations, if we assume negligible particle
evolution. In practice, both particle evolution or spatial inhomogeneity can produce similar signatures along a fall streak and
are not easily distinguishable. In the following, we will present real examples for spatially homogeneous and heterogeneous
situations and compare their real structure with the appearance in the THI.

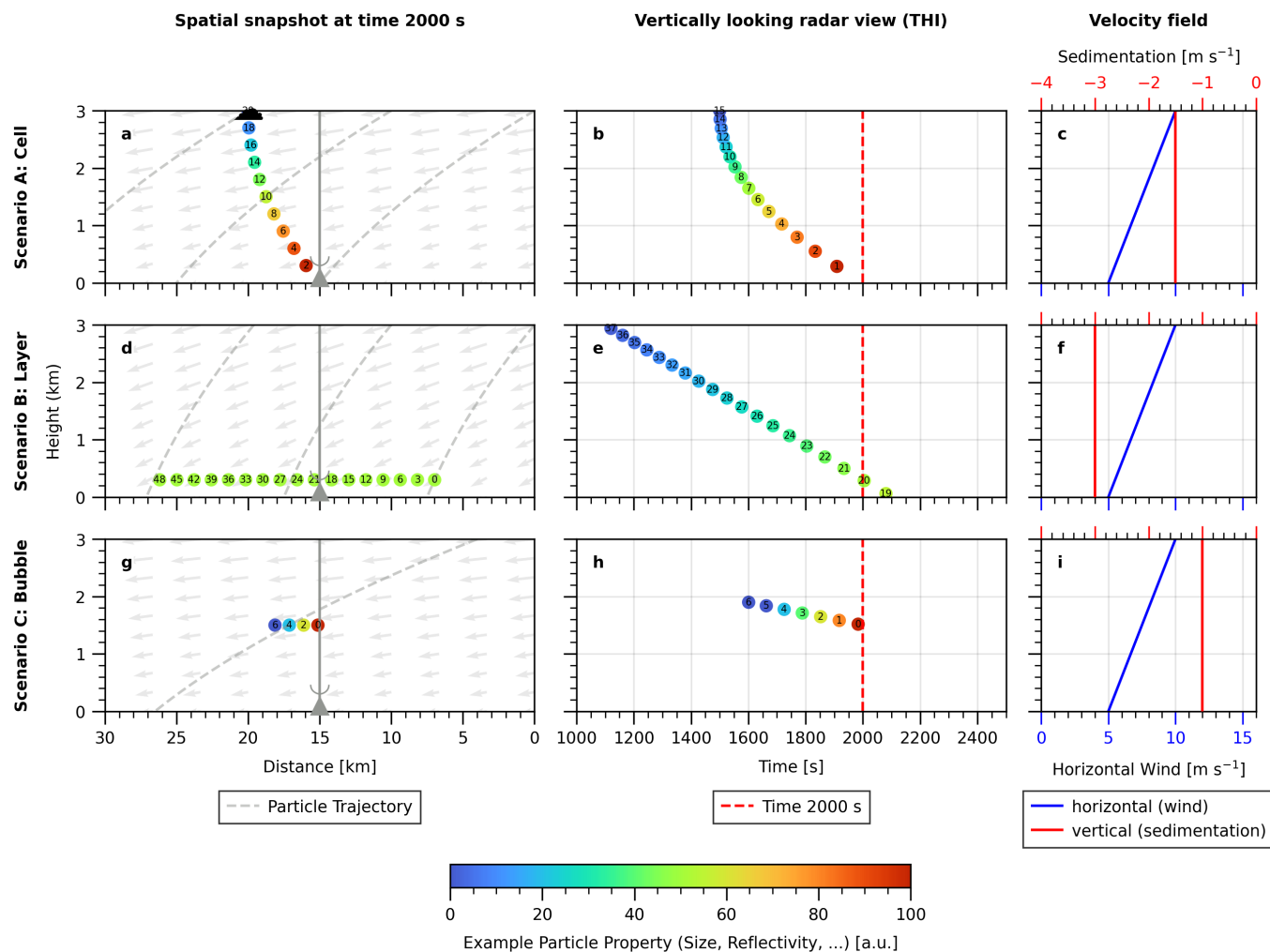


Figure 1. Simulation of three different particle seeding scenarios and their appearance in a THI. Please also consider the animated version of this illustration. First column ((a), (d), (g)): 2D x-z cross section of the atmosphere at time $t = 2000$ s. Particles are seeded at 3 km height and are constantly descending, while being advected with the background flow. Grey arrows show the combined velocity field (wind+sedimentation). Dashed lines show the particle trajectories. The particle color depicts an arbitrary particle property. This property can evolve as particles are descending, representing a process which is active on the particles (Scenario A and B), or stay constant (Scenario C). The particles have identity numbers for easier matching with the second column. The radar is located at $x = 15$ km at the surface. Second column ((b), (e), (h)): Time-height image (THI), as recorded by the radar in column one. The dashed red line shows the time of the snapshot in column one. Third column ((c), (f), (i)): Magnitude of the horizontal and vertical component of the velocity vector, i.e. horizontal wind speed and sedimentation speed. In all scenarios, the particles descend continuously, while the horizontal wind exhibits vertical shear.



3 Methods and measurements

125 3.1 Scan strategy and data acquisition

Measurements were performed in November 2024 in Munich, southern Germany by two Doppler cloud radars. The instruments are manufactured by METEK GmbH and installed on the roof of the Munich Institute for Meteorology. The first instrument operates at X-band at 10 GHz and continuously points vertically (Mróz et al., 2021). The second system operates at Ka-band at 35.2 GHz and is mounted on a dual-axis scanner (Görsdorf et al., 2015). This elevated position provides an almost unobstructed
130 field of view down to 2° above the horizon. The scanner allows for continuous and unrestricted rotation in azimuth.

Because our analysis relies on Doppler velocities from scanning measurements, accurate pointing is essential. We verified the pointing calibration of the Ka-band radar using the *SunscanPy* package (Ockenfuß et al., 2026b) within a precision of less than 0.1° . In addition, we corrected the data for a receiver-scanner time offset of 0.3 s.

To analyze the spatial extent and temporal evolution of an air parcel within a cloud, an ideal strategy would consist of
135 continuous three-dimensional volume scans. However, high-resolution volume scans require substantial time. For comparison, the operational volume scan of the German C-band radar network requires approximately 5 min while covering elevation angles only up to 25° . Given a typical cloud radar detection range of about 10 km and horizontal wind speeds on the order of 10 m s^{-1} , an air mass would advect beyond the radar's observable domain after at most one to two such volume scans.

To obtain more frequent snapshots of the evolving system, we therefore performed a sequence of range-height indicator
140 (RHI) scans, which provide vertically resolved cross sections through the cloud field. We selected the azimuth angle of the RHI such that the scanning plane is aligned parallel to the horizontal wind vector, i.e., the scans are performed along the mean wind direction (see Figure 2).

To determine the vertical profile of wind direction, we preceded each RHI sequence with a plan position indicator (PPI)
145 scan. PPI scans are conical scans at constant elevation angle off zenith and are sometimes also referred to as velocity azimuth display (VAD) scans. From these scans, we retrieved vertical profiles of horizontal wind speed and direction; details of the retrieval are provided in subsection 3.2.1.

Each scanning cycle consists of one wind PPI scan followed by 16 successive RHI scans. The antenna moves at 4° s^{-1} in
150 both azimuth and elevation. Consequently, a single PPI scan requires approximately 90 s. The RHI scans span elevation angles from 30° to 150° and take about 40 s each. At 90° elevation (zenith), the antenna decelerates and stops for 1 s to ensure at least one vertically pointing sample. Including processing time, the complete scan cycle repeats every 15 min.

We recorded radar moments and Doppler spectra with an averaging time of 1 s. At a pulse repetition frequency of 5 kHz, the system provides an unambiguous range of 27.7 km and a range resolution of 36 m. Doppler spectra are stored with a velocity resolution of 4.2 cm s^{-1} within an unambiguous Nyquist velocity of $v_{\text{ny}} = \pm 10.7 \text{ m s}^{-1}$. In this work, negative Doppler velocities correspond to movement towards the radar.

155 Initially, we performed the wind PPI scans at an elevation angle of 75° . At this configuration, horizontal wind speeds exceeding 41.3 m s^{-1} require Doppler de-aliasing. Therefore, we increased the PPI elevation angle to 80° for the second case study on 28 November.

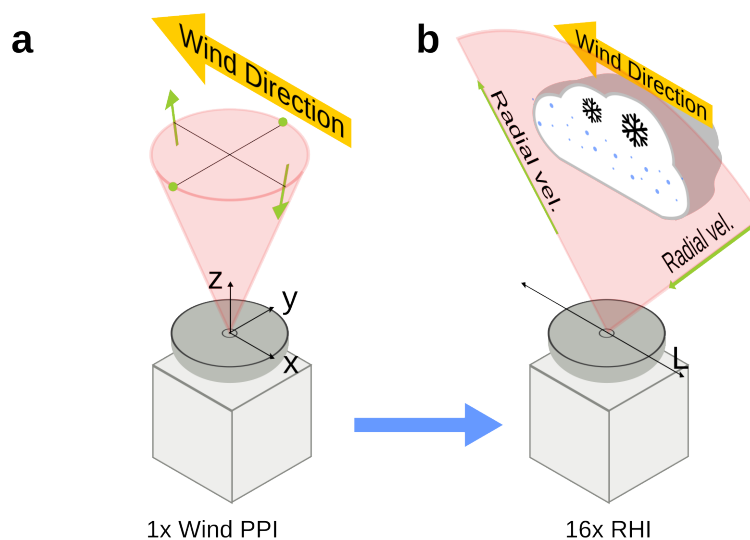


Figure 2. Illustration of the scan strategy. A PPI scan at high elevation (**a**) is performed to determine the horizontal wind direction and speed, followed by 16 consecutive RHI scans (**b**). The RHI scanning plane is aligned with the horizontal wind direction. The horizontal axis in the RHI plane is denoted by L . Thin, green arrows indicate the measured, radial Doppler velocity.

In most situations, wind direction varies with height. Because our focus is on snowflake riming, we align the RHI scans with the wind direction in the layer where riming is most likely to occur. Case studies (Vogl et al., 2022) and long-term statistics (Kneifel and Moisseev, 2020; Ockenfuß et al., 2025) show that riming occurs most frequently in the temperature range between 0°C and -15°C , with a strong increase in likelihood toward the melting layer. We therefore align the RHI plane with the median wind direction within a layer extending 400 m below and 1000 m above the melting layer. On days with surface temperatures below 0°C , the median wind direction between 0 m and 1000 m height is chosen.

To avoid the additional complexity of radar melting layer height retrievals, we instead use the height of the 0°C isotherm from the most recent ICON-D2 forecast of the German Weather Service (Zängl et al., 2014). The model output is available every three hours via the DWD Open Data Server (DWD, 2024) (variable `hzerocl`).

3.2 Scan processing

Doppler radars measure only the radial velocity of a target, i.e., the projection of the target's velocity vector onto the radar line-of-sight direction. In stratiform, non-convective weather systems, the horizontal advection of hydrometeors by the wind typically exceeds both the vertical air motion and the particle fall speed. As a result, the measured Doppler velocity exhibits characteristic spatial patterns that depend on the applied scan strategy.

For PPI scans, the Doppler velocity ψ as a function of azimuth angle ϕ at fixed range r follows a sinusoidal pattern. When the radar points directly into (away from) the horizontal wind, ψ is at minimum (maximum). When the beam is oriented



perpendicular to the wind direction, $\psi = 0$. This characteristic dependence has long been exploited for wind retrievals. For
175 example, Browning and Wexler (1968) illustrated the sinusoidal relationship and applied harmonic analysis to decompose the
azimuthal velocity variation. Matejka and Srivastava (1991) extended this approach by combining multiple PPI scans from a
single weather radar to separate horizontal divergence from vertical motion. Under the assumption of horizontal homogeneity,
they derived vertical profiles of vertical air velocity.

For our application, we adopt a more general framework that allows us to evaluate both PPI and RHI scans in a unified
180 manner. We define the Cartesian radar line-of-sight unit vector as

$$\mathbf{P} = (\sin(\phi) \cos(\theta), \cos(\phi) \cos(\theta), \sin(\theta))^T \quad (1)$$

where ϕ denotes the beam azimuth angle and θ the beam elevation angle. By definition, $\theta = 90^\circ$ corresponds to the zenith
direction.

We describe the particle motion with a general velocity model $\mathbf{M}_{\mathcal{P}}$:

$$185 \quad \mathbf{M}_{\mathcal{P}}(x, y, z, t) = \begin{pmatrix} u_{\mathcal{P}}(x, y, z, t) \\ v_{\mathcal{P}}(x, y, z, t) \\ w_{\mathcal{P}}(x, y, z, t) \end{pmatrix}, \quad (2)$$

where $u_{\mathcal{P}}$, $v_{\mathcal{P}}$, and $w_{\mathcal{P}}$ denote the velocity components in the x -, y -, and z -directions, respectively. In general, each compo-
nent may depend on the three-dimensional position (x, y, z) in space and time t .

The expected Doppler velocity at a given position and time is then

$$\psi_m = \mathbf{M}_{\mathcal{P}} \cdot \mathbf{P}. \quad (3)$$

190 Because this formulation involves three unknown velocity components but only a single measured Doppler velocity, the
problem is underdetermined. Therefore, in general it is necessary to reduce the degrees of freedom by parameterizing the
velocity field with a limited set of parameters \mathcal{P} .

Given a set of measured Doppler velocities $\{\psi_i\}_{i \in [1, N]}$, we determine the optimal parameter set by numerical optimization.
Specifically, we minimize the root-mean-square error between observations and model:

$$195 \quad \min_{\mathcal{P}} \left(\sqrt{\frac{1}{N} \sum_{i=1}^N (\psi_i - \mathbf{M}_{\mathcal{P}} \cdot \mathbf{P})^2} \right), \quad (4)$$

Minimization is done using Nelder-Mead simplex optimization (Gao and Han, 2010).



3.2.1 Plan Position Indicator (PPI) Scans

For the evaluation of the wind PPI scans, we assume a horizontally and temporally homogeneous velocity model $M_{\mathcal{P}}$ with three constant parameters, $\mathcal{P} = (u_0, v_0, w_0)$:

$$200 \quad M_{\mathcal{P}} = \begin{pmatrix} u_0 \\ v_0 \\ w_0 \end{pmatrix}. \quad (5)$$

We fit this model independently at each height level z using Equation 4. To demonstrate the equivalence of this formulation to the commonly applied sinusoidal fit for the evaluation of wind PPI scans, we can use Equation 3 to obtain:

$$\psi_m = u_0 \sin(\phi) \cos(\theta) + v_0 \cos(\phi) \cos(\theta) + w_0 \sin(\theta) \quad (6)$$

We introduce the horizontal wind speed s and wind direction d , defined by

$$205 \quad u_0 = s \sin(d) \quad v_0 = s \cos(d) \quad (7)$$

With this substitution, the Doppler velocity in Equation 6 becomes

$$\begin{aligned} \psi_m &= s \cos(\theta) (\sin(d) \sin(\phi) + \cos(d) \cos(\phi)) + w_0 \sin(\theta) \\ &= s \cos(\theta) \cos(\phi - d) + w_0 \sin(\theta) \end{aligned} \quad (8)$$

This expression is the well-known cosine wave pattern for ψ as a function of azimuth angle ϕ in PPI scans. The amplitude of the cosine wave is determined by the horizontal wind speed s and the elevation angle through $\cos(\theta)$. The phase shift of the wave is given by the wind direction d . A homogeneous sedimentation, subsidence or updraft w_0 introduces a constant offset proportional to $\sin(\theta)$.

3.2.2 Range Height Indicator (RHI) Scans

For RHI scans, any velocity component perpendicular to the scanning plane does not contribute to the measured Doppler velocity ψ . Consequently, the RHI geometry contains information only about the horizontal velocity component within the scanning plane, which we denote by γ .

We therefore define a model with two parameters $\mathcal{P} = (\gamma, w_0)$, where the horizontal wind vector lies entirely in the RHI plane specified by azimuth angle ϕ :

$$M_{\mathcal{P}} = \begin{pmatrix} \gamma \sin(\phi) \\ \gamma \cos(\phi) \\ w_0 \end{pmatrix}. \quad (9)$$



As for the PPI retrieval, we fit this model independently at each height level z . Substituting the parameterization into Equation 3 yields the analytical expression

$$\psi_m = \gamma \cos(\theta) + w_0 \sin(\theta). \quad (10)$$

Figure 3 illustrates this function. The blue curve shows the expected Doppler velocity for an RHI scan through a horizontally homogeneous wind field of 10 m s^{-1} . Variations in horizontal wind speed affect elevation angles close to the horizon stronger, as demonstrated in Figure 3a. In contrast, Doppler velocities within the elevation range 45° to 135° are predominantly sensitive to changes in the vertical velocity component, as shown in Figure 3b.

Figure 4 presents an observational example from an RHI scan recorded on 28 November 2024 in Munich. The radar natively samples data on an elevation (or time)-range grid (Figure 4a). To analyze and fit horizontal profiles, as shown in Figure 4b and Figure 4c, we regrid each beam from range coordinates to fixed height levels using nearest-neighbour selection.

The grey curve in Figure 4b shows the raw (folded) Doppler velocity ψ_f . To correct for velocity aliasing, we first fit $M_{\mathcal{P}}$ to the near-zenith elevation range between 80° and 100° , which is unaffected by folding. We then use the retrieved horizontal wind speed to compute the approximate Doppler velocity ψ_a at all elevation angles. Integer multiples n_ν of the Nyquist interval $\nu = 21.4 \text{ m s}^{-1}$ are subsequently added to or subtracted from ψ_f to minimize the difference to ψ_a . The optimal n_ν can be calculated as:

$$n_\nu = \text{round} \left(\frac{\psi_a - \psi_f}{\nu} \right). \quad (11)$$

The unfolded Doppler velocity is shown as the blue curve in Figure 4b. Fitting $M_{\mathcal{P}}$ to this unfolded profile yields the orange curve. The model reproduces the measurements well except at the elevation angles close to the horizon, where the observed Doppler velocities systematically exceed the fitted curve. If such a pattern persists over multiple RHI scans, it indicates the presence of an unaccounted acceleration or deceleration in the horizontal wind speed, as shown as follows.

We introduce a linear term to the in-plane wind component γ as

$$\gamma = \gamma_0 + \lambda L, \quad L = \frac{z}{\tan(\theta)}. \quad (12)$$

where L denotes the horizontal distance from the radar. The resulting expression for the modeled Doppler velocity becomes

$$\psi_m = \gamma_0 \cos(\theta) + \lambda z \frac{\cos^2(\theta)}{\sin(\theta)} + w_0 \sin(\theta). \quad (13)$$

The influence of the parameter λ on ψ_m is illustrated in Figure 3c. Note how a positive (negative) change in λ causes the curves to increase (decrease) for the low and high elevation angles near the horizon, similar to the pattern observed in Figure 4b.

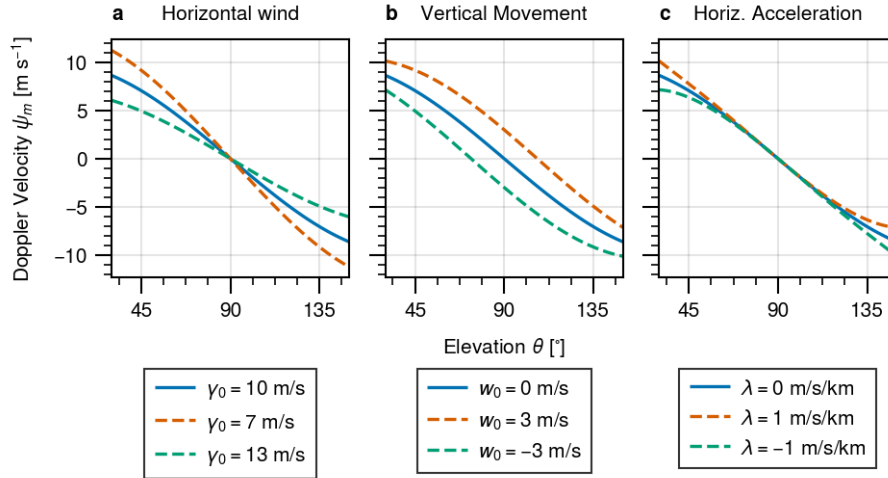


Figure 3. Radial Doppler velocity as a function of beam elevation angle, calculated according to Equation 13. Blue line (the same in all panels): Doppler velocity from a constant horizontal wind of $\gamma_0 = 10 \text{ m s}^{-1}$. **(a)** Influence of the horizontal wind strength γ_0 on the Doppler velocity. **(b)**: Influence of the average vertical velocity w_0 . **(c)**: Influence of the linear horizontal variability λ .

245 Figure 4c shows the elevation profile at a height of 3.1 km. At this level, deviations from the fitted model remain near zenith. In the following, we fit Equation 13 to all height levels and attribute any remaining deviations to variations Δw between the mean vertical velocity w_0 and the actual vertical velocity w :

$$w = w_0 + \Delta w. \tag{14}$$

The measured Doppler velocity can then be written as

250
$$\psi = \psi_m + \Delta w \sin(\theta). \tag{15}$$

Solving Equation 15 for Δw , we can write Equation 14 as:

$$w = w_0 + \frac{\psi - \psi_m}{\sin(\theta)}. \tag{16}$$

This retrieved vertical velocity field w is shown in Figure 4d.

3.3 Spectra processing

255 Radar Doppler spectra are affected by horizontal wind in the same way as the mean Doppler velocity (which, in fact, the radar signal processor derives from the spectra). In Figure 5a, we present an example spectrogram recorded at an azimuth angle of 137° . The spectrum exhibits signatures of velocity folding, wind-induced shifting and distortion.

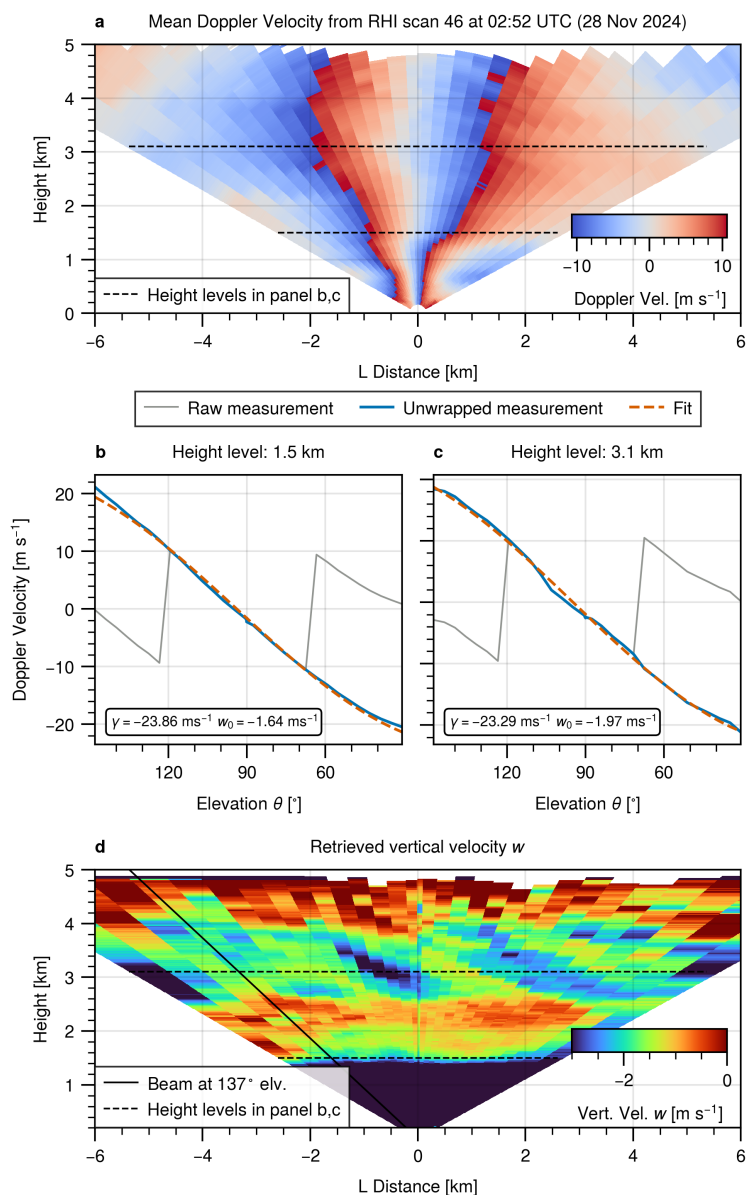


Figure 4. (a): Raw, i.e. folded, Doppler velocity on the native elevation-range grid, as recorded from a single RHI scan on November 28, 2024. (b), (c): Doppler velocity along two horizontal cross sections of panel (a). Raw measurements are shown in grey, unfolded measurements are shown in blue. The dashed, orange line depicts a fit of the constant wind model (Equation 10) to the unfolded data. The fit parameters are shown in the box. (d): Vertical velocity w retrieved according to Equation 16. The spectrogram in Figure 5 was recorded along the beam highlighted by the black, solid line.

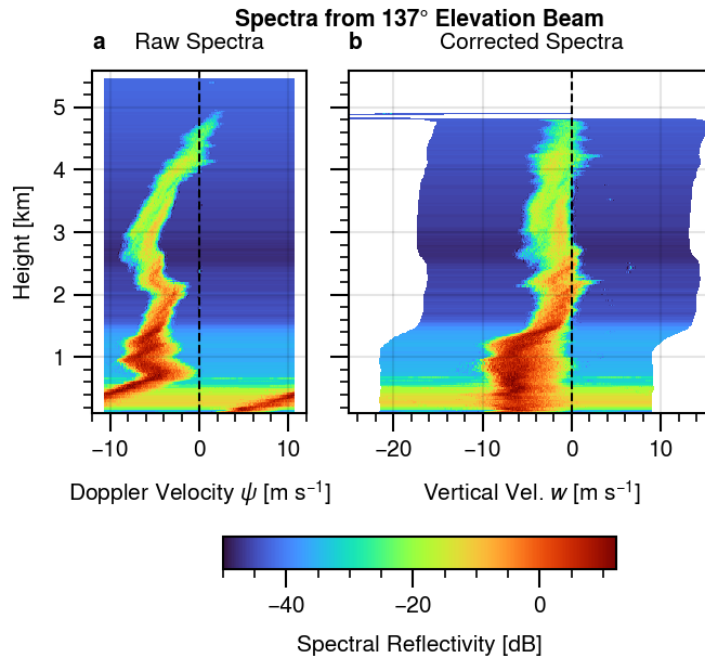


Figure 5. Example spectrograms recorded along the highlighted beam in Figure 4d. **(a):** Uncorrected measurements. **(b):** Unfolded, undistorted and unshifted version of the spectrogram in (a), as described in subsection 3.3.

After retrieving $M_{\mathcal{P}}$ from the RHI scan, we use Equation 11 and Equation 16 to unfold and correct the individual Doppler spectrum bins, analogous to the correction applied to the MDV. The corrected spectrum is shown in Figure 5b. Notably, the detectable velocity range in Figure 5b is approximately 30 m s^{-1} , which substantially exceeds the actual velocity range of 21.4 m s^{-1} in Figure 5a. This apparent increase in Nyquist velocity arises because in slanted beams, the projected magnitude of vertical velocities is reduced by the corresponding trigonometric factor $\sin(\theta)$.

For the analysis of the first case presented in subsubsection 4.1.3, we identify distinct spectral peaks and cluster them into vertically continuous modes within the spectrogram. We describe the details of the peak detection and mode identification algorithms in Appendix A.

3.3.1 Introducing Spectral Column Vertical Profiles (SCVP)

Murphy et al. (2020) introduced the Column Vertical Profile (CVP) technique, which enables the construction of relatively high-resolution vertical profiles from multiple slanted radar beams. The method projects radar moments from a defined sector onto a common vertical line, thereby synthesizing a vertical profile at a given surface location.

We extend this concept by proposing the spectral Column Vertical Profile (SCVP), which incorporates the full Doppler spectral dimension. By mapping the entire Doppler spectra from within a selected sector onto a vertical line, we construct



vertical spectrograms that approximate the measurements of a vertically pointing radar located at the corresponding surface position.

We perform the projection following Murphy et al. (2020), with one important modification. Rather than using the intermediate elevation angle to separate contributions from two adjacent beams with elevation angles θ_1 and θ_2 , we introduce a distance-optimized separation angle θ_s , defined as

$$\theta_s = \arctan\left(2 \frac{\tan\theta_1 \tan\theta_2}{\tan\theta_1 + \tan\theta_2}\right). \quad (17)$$

This angle minimizes the vertical distance mismatch between adjacent beams and can also be applied to optimize the traditional CVP technique. Appendix B illustrates the underlying geometric problem and provides a detailed derivation.

280 4 Results

4.1 Example of a spatially homogeneous riming case

On 21 November 2024 at 18 UTC, the surface low "Caetano" was centered over central France with a core pressure of approximately 987 hPa (compare Figure D1). Between 18 UTC and 00 UTC, the surface low moved eastward across northern Italy toward northern Croatia and Slovenia. In southern Germany, horizontal pressure gradients were very weak. A shallow layer of cold air had previously been advected into the region by a weak northeasterly flow. As the low-pressure system progressed eastward across southern Europe, it induced overrunning of milder, moist Mediterranean air over the cold near-surface air mass in southern Germany. Light snowfall began in the Munich area around 16:30 UTC, intensified slightly from about 18:30 UTC, and gradually diminished during the second half of the night leading up to 22 November.

4.1.1 THI perspective with continuous fall streaks

290 Between 20:20 UTC and 20:50 UTC, the vertically pointing X-band radar recorded three clearly visible fall streaks with enhanced vertical Doppler velocity up to 3.5 m s^{-1} , as can be seen in Figure 6a. Figure 6b shows the vertical profile of the horizontal wind derived from PPI scan number 2 of the Ka-band radar. The temporal sequence and numbering of the scans are presented in Figure 6c. The azimuthal orientation of the RHI scanning plane compared to the wind profile is indicated in Figure 6d.

295 The wind direction exhibits vertical shear, i.e. it veers from southeasterly directions near the surface to westerly directions at higher altitudes and increases in speed. This shift is consistent with the overrunning of the milder, moist Mediterranean air mass. As a result, no unique and well-defined along-wind direction exists for the RHI-scan. Based on the average wind direction around the melting layer or surface, the processing software selected an azimuth angle of 109° for RHI scans number 29 to 44.

4.1.2 Using RHI scans to reveal the spatial structure

300 Figure 7 presents the situation from the perspective of the scanning radar. The fall streak previously seen in the THI appears as an extended layer of faster-falling particles in the RHI. This situation therefore closely resembles the conceptual scenario B

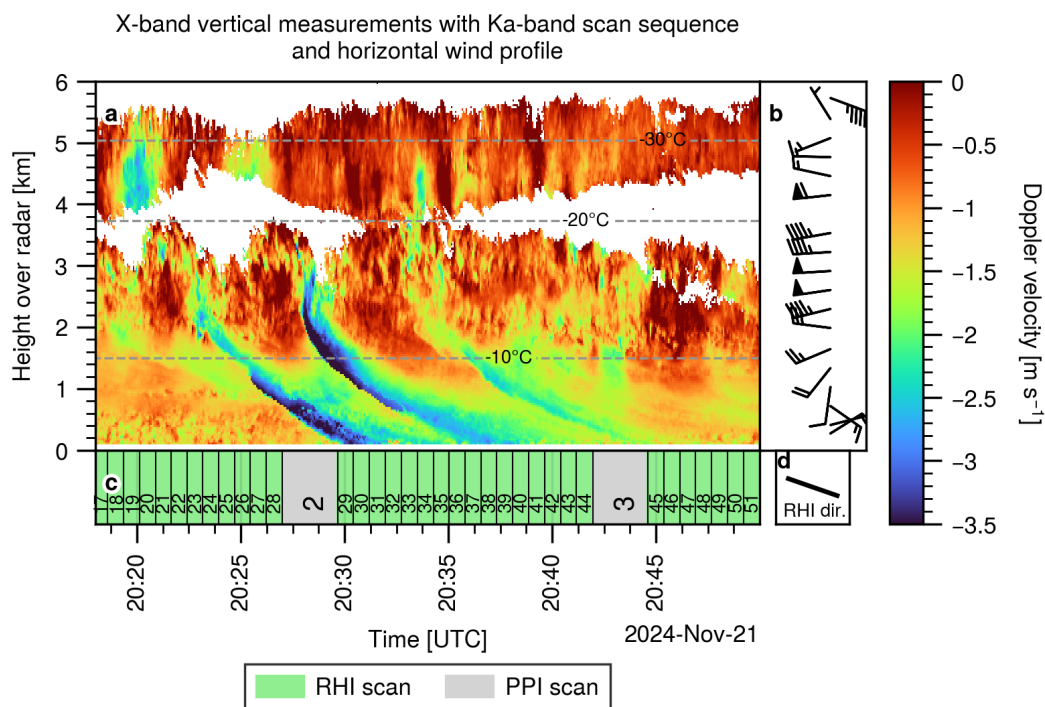


Figure 6. (a): THI, recorded by the vertically pointing X-band radar. The dashed lines show isotherms, taken from the ERA 5 reanalysis (Hersbach et al., 2020). (b): Vertical wind profile, as derived from PPI scan number 2. The barbs indicate the wind direction and wind speed in knots. (c): The scan sequence of the Ka-band radar, alternating between RHIs (green) and PPI (grey). (d): Indicates the orientation of the RHI scanning plane (similar to the wind barbs, e.g., horizontal would mean along East-West).

shown in Figure 1, where a thin, extended, homogeneous layer of rimed particles descends continuously (Figure 1d), creating a thin streak in the THI (Figure 1e). The layer spans at least 4 km in the horizontal (limited by the distance covered by the scan) and it descends continuously over time.

305 Only the first scan in Figure 7a exhibits significant variability within the layer. When interpreting this structure, we must consider that the slanted beams at the beginning and end of the RHI are only weakly sensitive to the vertical velocity component. Consequently, the regions of enhanced downward velocity around ± 2 km horizontal distance, highlighted by the red ellipses, are most likely caused by fluctuations in the horizontal wind and turbulence during the formation phase of the layer.

At the beginning of the time series shown in Figure 7a-c, the descent of a preceding layer remains visible near the surface
310 (see also Figure 6). Similarly, toward the end of the sequence in Figure 7h, the formation of the next layer becomes apparent at a height of approximately 2 km.

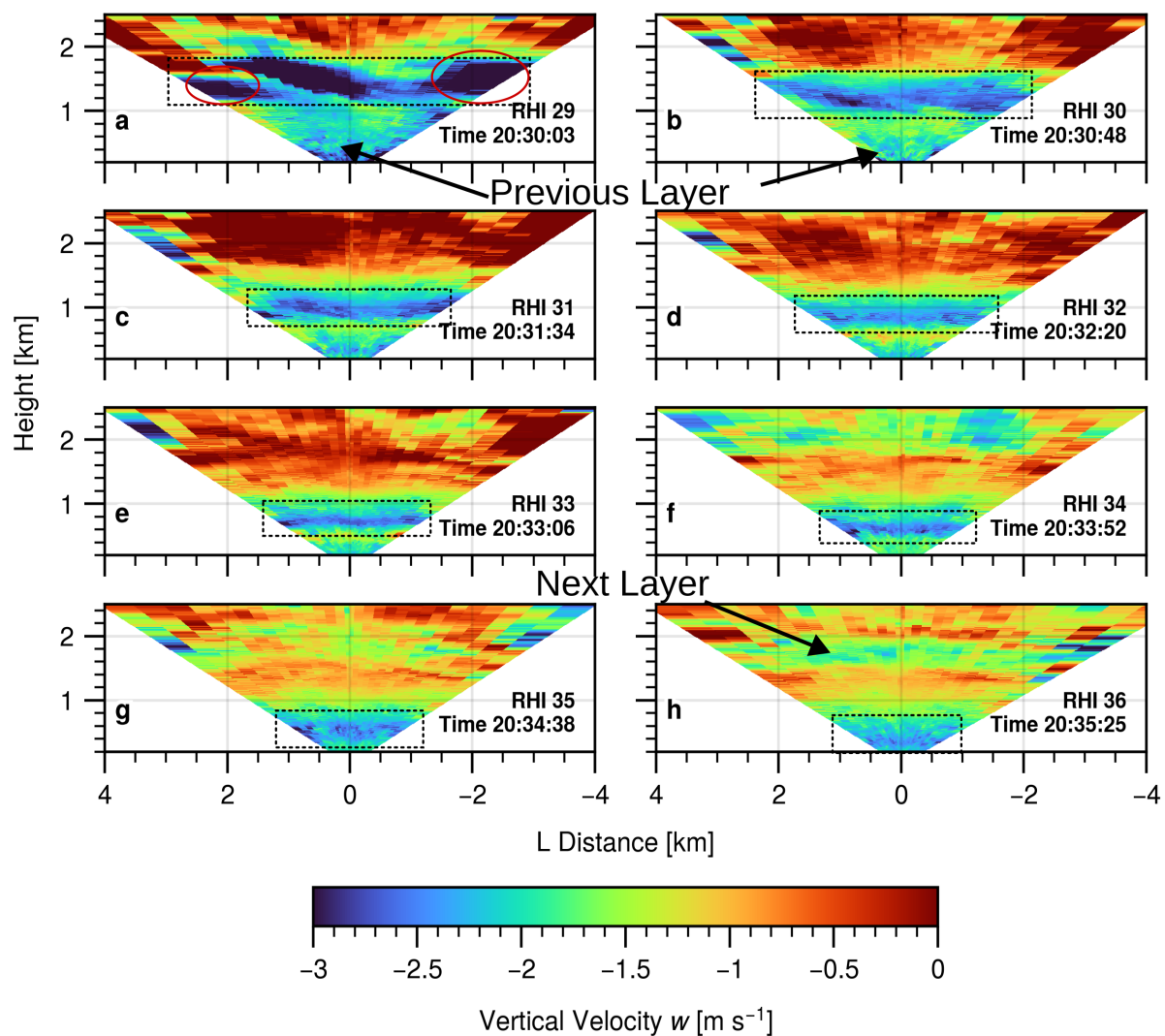


Figure 7. Spatial reconstruction of the vertical velocity field, as in Figure 4d. (a) to (h) show the series of RHI scans from number 29 to 36, as also illustrated by the scan sequence in Figure 6c. The black box highlights the descending layer of rimed particles. The red circles in (a) show regions of enhanced velocity, which may be attributed to changes in the horizontal wind speed.

4.1.3 Identification of rimed particles in slanted Doppler spectra

To prove that the layer of enhanced vertical velocity in the RHI scans is caused by rimed particles, we analyze the corresponding radar Doppler spectra in Figure 8. Panels b-h show spectrograms from different elevation angles of RHI 32, processed as described in subsection 3.3

315

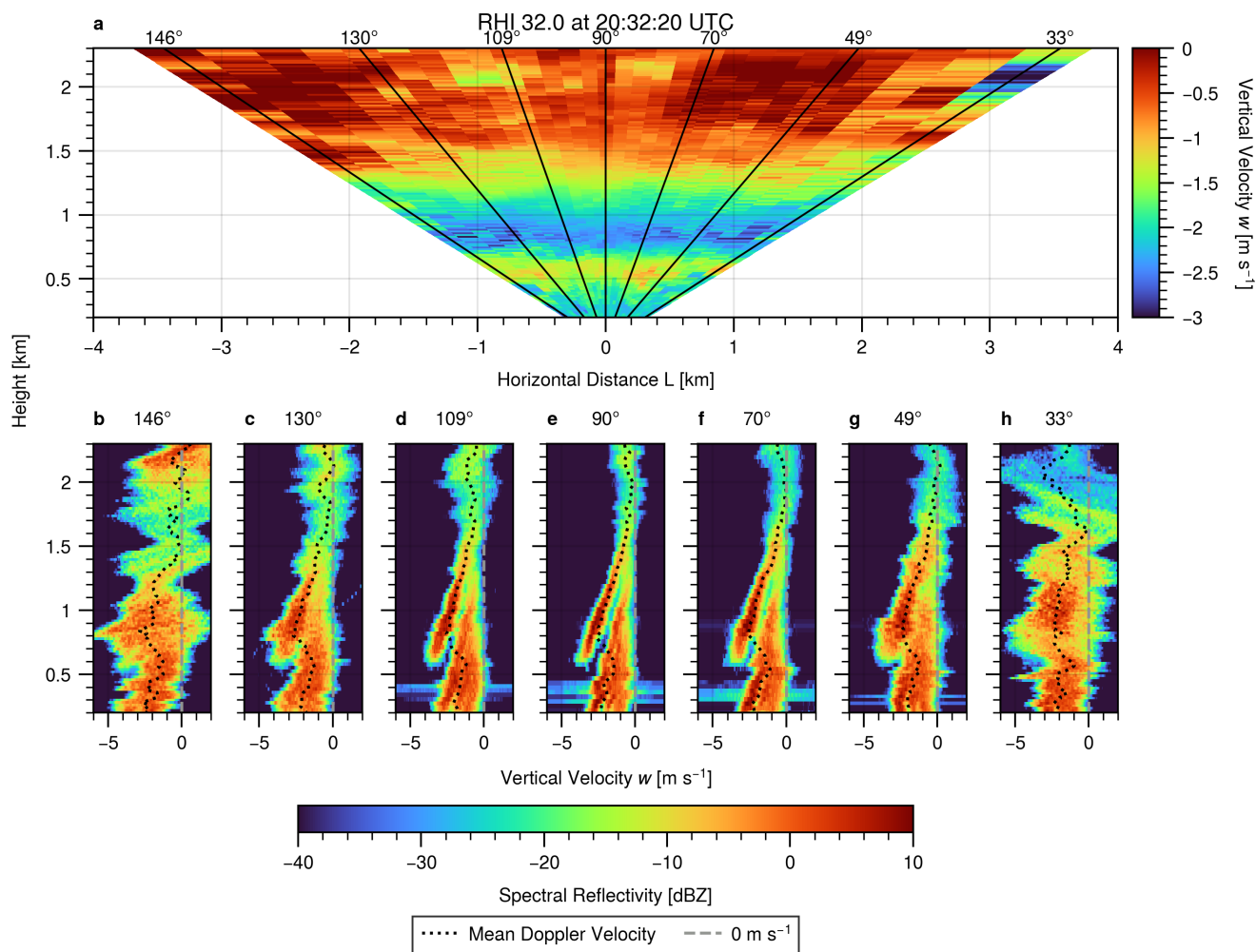


Figure 8. **a:** Vertical velocity field (same as Figure 7d). The black lines denote the selected beams in (b) to (h). **(b) to (h):** Corrected spectrograms along selected beams. The black dotted line follows the mean Doppler velocity (first moment) of the spectra, as shown in (a).

In the vertically pointing beam (Figure 8e), two distinct spectral modes are clearly visible at approximately 1 km height, indicating the presence of two separate particle populations. The slower-falling mode corresponds to unrimed snow, which persists throughout the entire column. The faster-falling mode represents rimed particles descending through the snow.

These two spectral modes remain distinguishable up to an offset angle of about 40° from the vertical. At larger offsets, around 60° , the reconstructed spectrograms become increasingly noisy due to the reduced sensitivity of the measured Doppler velocity to the vertical velocity component. Although the rimed-particle mode still manifests as an enhancement in MDV, a clear peak separation from the snow mode is no longer possible.



4.1.4 Analyzing rimed particle evolution

As evident from Figure 7, the assumption of a horizontally homogeneous distribution of the rimed particles is fulfilled for this
325 case. Only under these conditions, we can focus on the 90° zenith spectrograms from subsequent RHIs and interpret their
temporal evolution as representative of the particle evolution itself, as it is commonly done in THI based process studies (e.g.
Kalesse et al., 2016; Pfitzenmaier et al., 2017). Note that the observed particles are not identical in each vertical spectrogram.

In Figure 9, we apply the peak and mode finder described in Appendix A to separate rimed particles from the background
snow. Figure 9a-c show three temporal snapshots, with the riming mode of interest highlighted by stars. In Figure 9a, close to
330 the surface, an additional fast secondary mode appears, representing the remainder of a previous riming layer. The black lines
indicate the upper, lower, and left boundaries of the riming mode in the spectrograms.

Figure 9d illustrates the temporal evolution of the upper and lower boundaries of the riming mode. The riming layer steadily
descends, while the lower boundary—composed of the most strongly rimed and fastest particles—continuously advances
relative to the upper boundary. This is a result of density sorting within the layer.

335 Figure 9e shows the evolution of the left boundary of the mode, corresponding to the velocity of the fastest particles. We
find no indication of acceleration or further increase in rime mass during descent. The slight deceleration toward the surface
may result from increasing air density. As a consistency check, we can also estimate the particle velocity from the descent of
the riming mode lower boundary between subsequent RHIs, as shown in Figure 9d. This yields a velocity of 3.1 m s^{-1} , which
is slightly lower but generally consistent with the mean velocity of 3.6 m s^{-1} inferred for the fastest particles from the Doppler
340 spectra left edge. This implies that the detected Doppler velocities are consistent with the total evolution of the system.

4.1.5 Can vertical observations and backward trajectories confirm the derived spatial structure?

As we have seen, by removing the horizontal wind contribution from RHI scans, we can directly observe the spatial distribution
of rimed particles. As we have discussed previously, a THI can only provide us with reliable information about the spatial
appearance of a scene, if we assume negligible particle evolution, since spatial structure and time evolution are intrinsically
345 mixed in a THI view. For our current case, we have seen that the rimed particles descend continuously. This opens up the
possibility for a consistency check: Under the assumption of constant sedimentation, we can attempt to reconstruct the spatial
distribution of the rimed particles, using only information from vertical observations. We would then expect the reappearance
of the characteristic layer structure.

To this end, we focus exclusively on the vertical spectra, which is what we would obtain from a THI. We isolate the rimed
350 particles from the background snow (highlighted by stars in Figure 9a-c) and place them in a three-dimensional domain with
the initial conditions for position, height, and time according to the THI. By reversing time, we reconstruct particle backward
trajectories over the Munich city center, assuming that their vertical velocity is constant. For the horizontal wind advection, we
use the wind field retrieved from the wind PPI scan.

Figure 10 shows a snapshot of the simulation. (please see also the provided animation). For reference, Figure 10a shows a
355 THI section from the X-band radar, similar to Figure 6. Figure 10b presents a side view of the simulation domain 100 s before

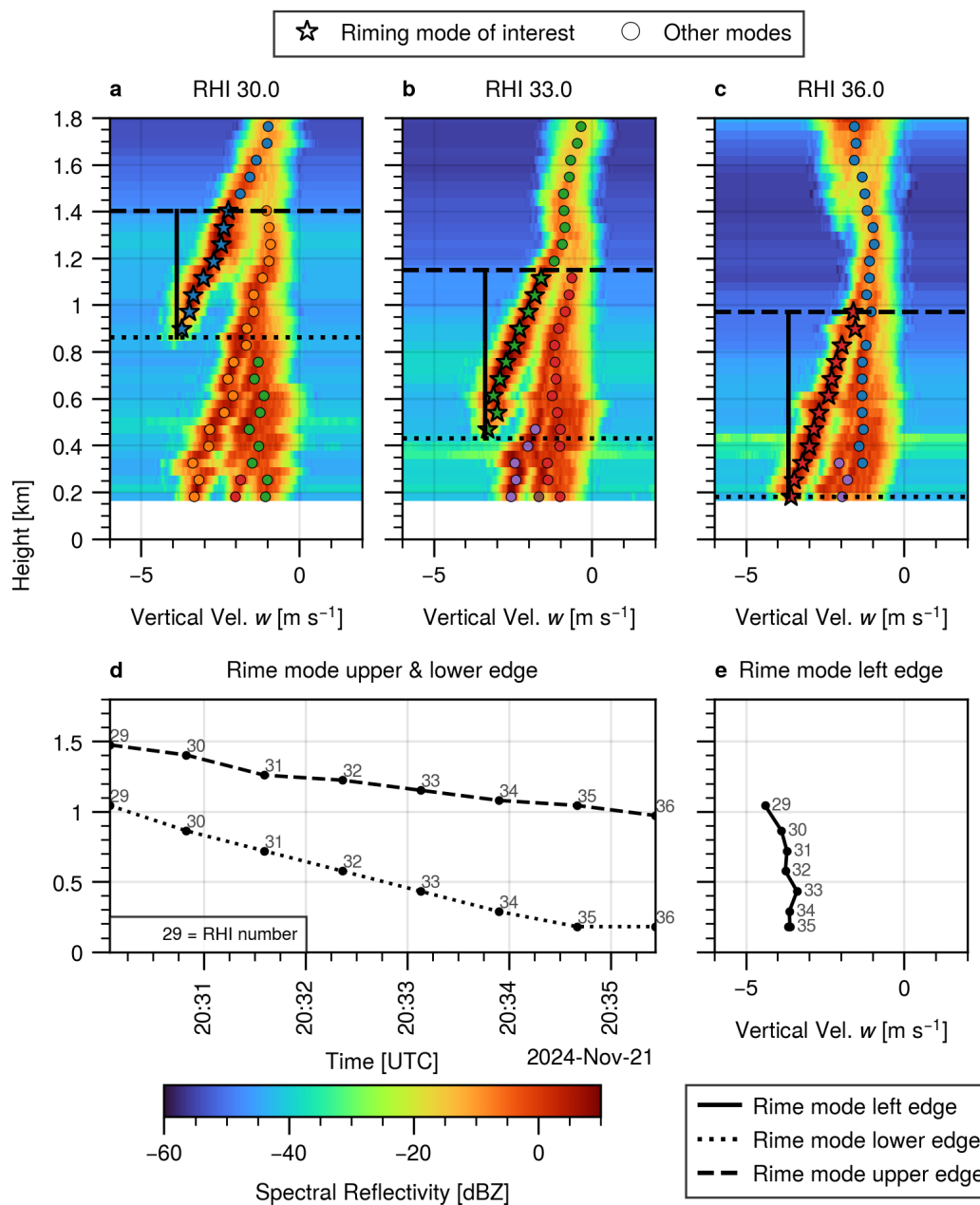


Figure 9. (a), (b), (c): Spectrograms along the vertical beam of selected RHI scans. Dots highlight peaks detected by the peak finder algorithm. Peaks belonging to the same mode according to the mode finder algorithm have the same color. Stars highlight the riming peaks/mode. The dashed, dotted and solid line depicts the upper, lower and left edge of the riming mode, respectively. (d): Time evolution of the upper and lower edge of the rime mode. (e): Height (and therefore time) evolution of the left edge velocity of the rime mode.



the first RHI scan happened. As is visible, at this time the backward trajectories of all particles observed over the radar during a 6 min period converge into a single layer of around 300 m thickness. This independently confirms the layer structure inferred from the scans in Figure 7.

The top-down view in Figure 10c reveals that the rimed particles observed in the THI originated from a region up to 4 km southwest of the radar. Moreover, the faster particles stem from a markedly different area than the slower ones. This demonstrates that particles appearing simultaneously above the radar in a THI may in fact originate from spatially very different source regions.

4.2 Example of a spatially inhomogeneous riming case

One week later, on 28 November 2024 at 00 UTC, the surface low “Conall” was centered over northern Germany with a core pressure of approximately 998 hPa (compare Figure D2). Over central Germany, the corresponding surface cold front was oriented nearly parallel to the westerly upper-level flow. Ahead of the front, southern Germany was situated within the broad warm sector of the cyclone. A southwesterly flow advected mild and moist Atlantic air into the region, within which a prefrontal precipitation band developed. During the second half of the night, both the prefrontal band and the cold front progressed slowly southeastward. The prefrontal precipitation band crossed the Munich area between approximately 01 and 04 UTC.

4.2.1 Disappearing fall streaks in the THI

Around 03 UTC, the vertically pointing X-band radar revealed pronounced riming fall streaks (Figure 11a). As in Case 1, these streaks originated at temperatures between -10°C and -15°C near the turbulent cloud-top region and extended downward. In contrast to Case 1, however, several streaks did not reach the ground or the melting layer but appeared to terminate at approximately 2.6 km height.

Under the classical fall streak interpretation assuming horizontal homogeneity, such behavior would suggest deceleration or disappearance of the rimed particles. The immediate microphysical interpretation would be a reduction in particle mass or density due to strong evaporation, or alternatively a local updraft producing an apparent Doppler velocity slowdown. However, as demonstrated in Figure 1, a horizontally inhomogeneous situation, such as the “Bubble” Scenario C, can likewise produce a “disappearing” fall streak in the THI.

4.2.2 Using RHI scans to reveal the riming spatial distribution

The RHI scans resolve the ambiguity in the THI. Figure 12 presents the retrieved vertical velocity fields from RHI scans 44 to 48 of Case 2. Compared to Case 1, the field exhibits stronger horizontal heterogeneity. In Figure 12a, we identify a localized region of rimed particles, consistent with the idealized “Bubble” Scenario C. In this case, the horizontal wind speed was about 20 m s^{-1} between 2 km to 4 km height, stronger than in Case 1, but with negligible shear in magnitude or direction (Figure 11b). Because the RHI plane was aligned with the wind, we observe the bubble advecting over the radar during the

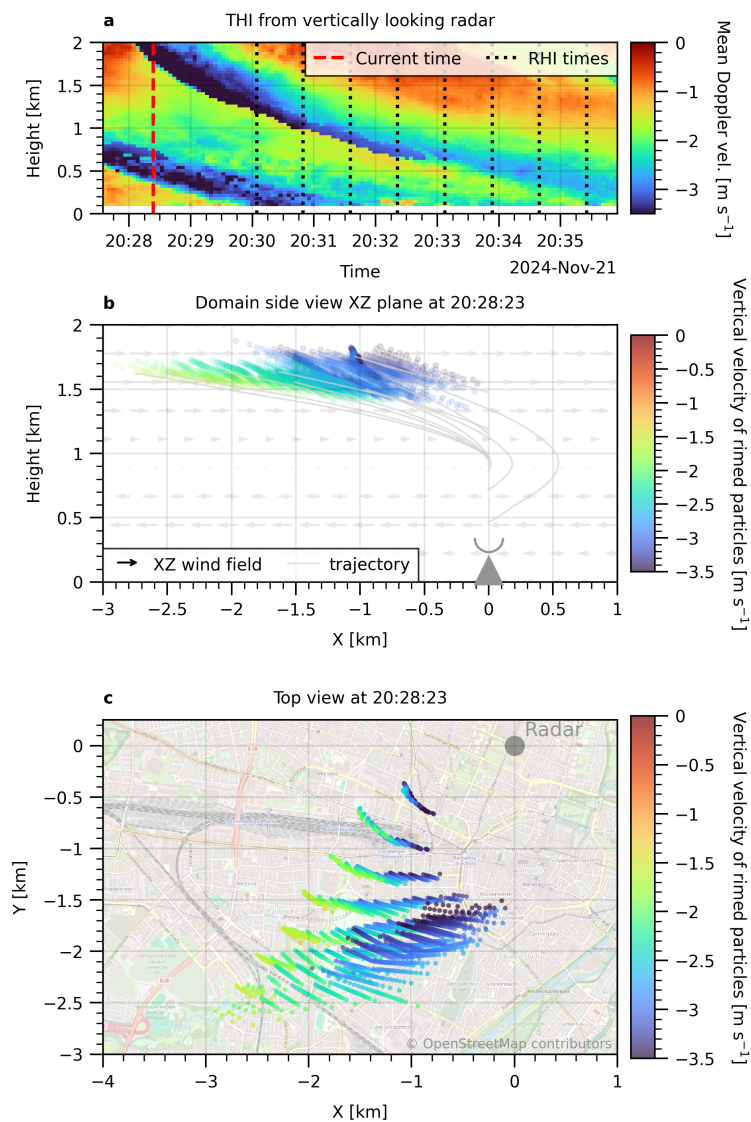


Figure 10. Backward trajectories of rimed particles. Please also consider the animated version of this illustration. **(a):** THI from X-band radar, as shown in Figure 6a. Black lines denote the times of the RHI scans. The advected particles are taken from the vertical beam of each scan. The red line marks the time of the snapshots in **(b)** and **(c)**. **(b)** Side view of the 3D domain (XZ projection). Arrows indicate the wind in X direction. Grey lines show the (XZ-projected) particle trajectories. **(c):** Top view of the 3D domain (XY projection). The background shows a map of the Munich city center.

subsequent four RHIs (first column in Figure 12), thereby producing the partial fall streak in the THI. The spatial fields show no indication of particle deceleration.

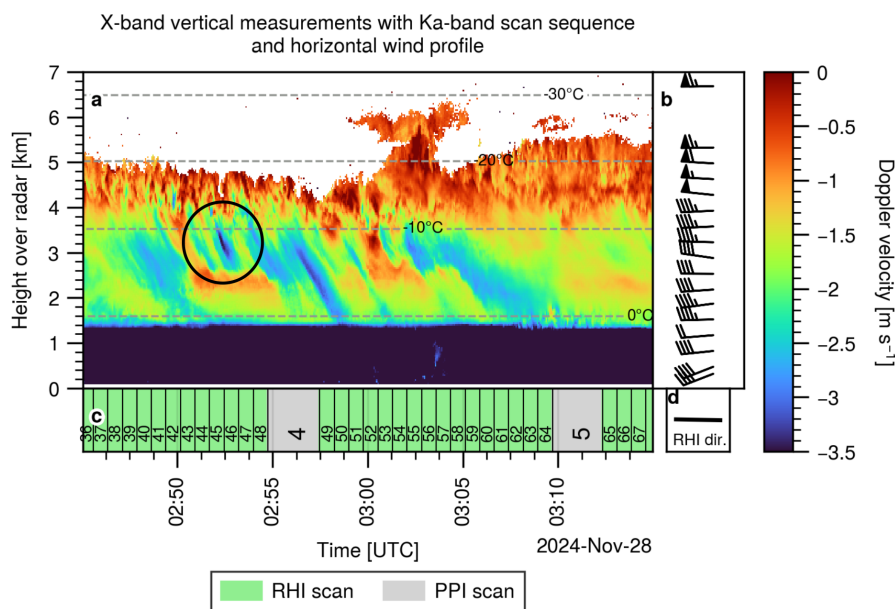


Figure 11. Same as Figure 6, but for Case 2 on November 28, 2024. The black circle in (a) highlights the partial fall streak, which will be analyzed in subsection 4.2.2.

4.2.3 Riming appearance in spectrograms along a single, slanted beam

390 As in Case 1, we separate rimed particles from the background snow using Doppler spectra. However, due to the horizontal heterogeneity, vertically pointing spectra alone are insufficient to capture the particle evolution. Instead, we follow the bubble in a Lagrangian framework and analyze the reconstructed spectra from the slanted beams intersecting the bubble. These spectra are shown in the second column of Figure 12. The rimed particles appear as a faster-falling mode at approximately 3.5 km height. From Figure 12b to j, this riming mode becomes vertically elongated, similar to Case 1 (Figure 9). This elongation may
 395 indicate size sorting, but the viewing geometry also affects the spectral appearance in this case. As illustrated in Figure 12a, the bubble has an elliptical shape. The 65° beam in Figure 12a intersects it along the semi-minor axis, whereas in RHI 48 (Figure 12i) the 134° beam intersects it along the semi-major axis. This contributes to the elongation. To mitigate this geometric effect, we propose the spectral CVP technique to generate spectrograms along a virtual vertical line.

4.2.4 Creating spectral CVP from multiple slanted beams for the lagrangian tracking of a single particle population

400 Figure 13a-c present three exemplary vertical profiles through the rime bubble, constructed by projecting data within a horizontal distance of up to 200 m onto a virtual vertical line. For each profile, the corresponding SCVP is shown in Figure 13d-f.

As in Figure 9, we identify and analyze the rimed particles from the spectra. However, the spectral peaks are less distinct than in Case 1. We therefore apply a reflectivity threshold of 10 dBZ, which captures the rime mode well in this case (contours

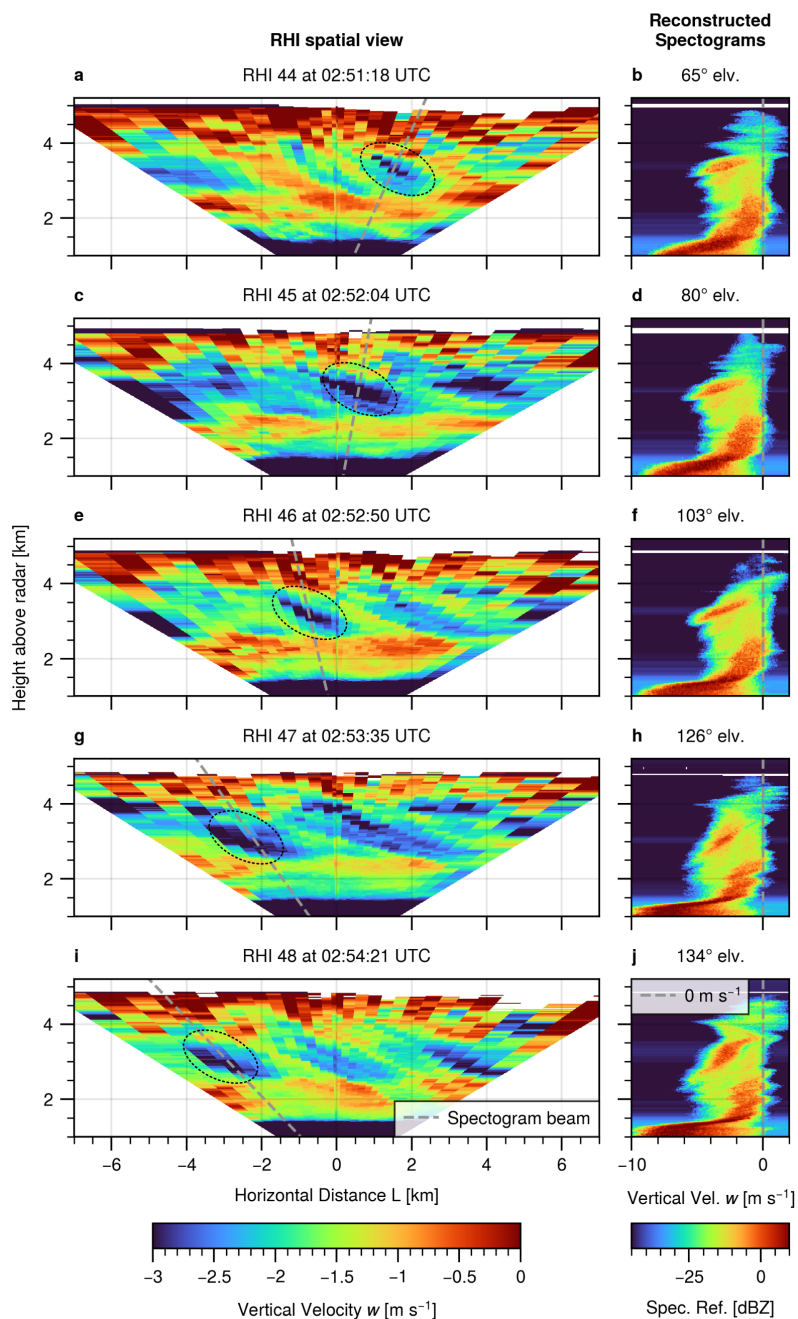


Figure 12. Left column: Spatial reconstruction of the vertical velocity field for Case 2 on November 28, 2024. The spectograms in the right column are taken along the grey, dashed beam. The black, dashed ellipses show the location of the bubble of rimed particles. **Right Column:** Corrected spectograms along slanted beams



in Figure 13d-f), instead of using the peak-finder algorithm. Figure 13g shows the leftmost spectral edge within the height
405 range where rimed mode is detected. As in Figure 9, we find no significant acceleration or deceleration of the fastest particles.
With fall velocities of approximately 5 m s^{-1} , they are about 1 m s^{-1} faster than in Case 1.

In contrast, the upper and lower boundaries of the rime mode exhibit a downward trend, as shown in Figure 13h, due to the
descend of the rimed particles through the cloud. Similar to Figure 9, we observe density sorting, indicated by the increasing
separation between upper and lower edges over time while both descend. A linear fit to the time evolution of the upper and lower
410 mode boundary in Figure 13h allows us to quantify the downward trend, revealing velocities of -1.2 m s^{-1} and -2.9 m s^{-1} for
the upper and lower edge, respectively. This is consistent with the velocities inferred directly from the spectrogram's velocity
axis.

5 Discussion

5.1 Insights about the spatial structure and evolution of riming

415 In our study, we presented two riming cases. The first case corresponds well to the layer scenario B in Figure 1, while the
second case exhibits characteristics of the bubble scenario C in Figure 1.

In Case 1, we observe multiple extended, stratiform layers of rimed particles forming near cloud top and continuously
descending toward the surface. This behavior agrees with the synoptic situation, which indicates slow, large-scale uplift of a
warm and moist air mass over colder surface air, potentially creating an extended reservoir of supercooled liquid water. In
420 Figure 6, a distinct two-layer cloud system is visible. Riming is initiated when ice crystals from the upper feeder cloud seed
the upper part of the lower cloud layer.

Case 2, in contrast, features a strong and vertically homogeneous wind profile but heterogeneous riming. No seeder cloud is
detected. Instead, riming appears to initiate directly within the turbulent cloud-top layer, possibly through generating cells that
form localized pockets of supercooled liquid water, as described by Houze and Medina (2005).

425 Despite these differences, both cases share a common feature: riming forms within a relatively thin layer near cloud top, and
we do not detect additional riming as particles fall through the underlying background snow. This finding agrees with Ockenfuß
et al. (2025), who analyzed more than 10 years of vertical profile data. They found maximum rime mass deposition rates near
the top of riming events and that on average, most of the increase in rime mass fraction occurs within the first 500 m.

Because our analysis represents a case study, the frequency and generality of the observed phenomena remain uncertain.
430 Nevertheless, several indications suggest that riming in stratiform clouds typically occurs on larger spatial scales, resembling
Case 1. From the authors' experience, "disappearing" riming fall streaks in THI are rare; most extend to the surface or melting
layer. This impression is supported by the statistics of Ockenfuß et al. (2025), which show that the lowermost edge of riming
signatures in THI is almost always located near 0°C .¹

¹Ockenfuß et al. (2025) cluster the signatures in the THI along time into connected riming "events". Depending on the cluster algorithm, all fall streaks in
our Case 2 (Figure 11) may be seen as belonging to one event. Since around 02:57 UTC, one fall streak reaches until the melting layer, the combined event
lower edge could also be located around 0°C . However, we can conclude from their statistics that isolated, disappearing riming fall streaks are very rare.

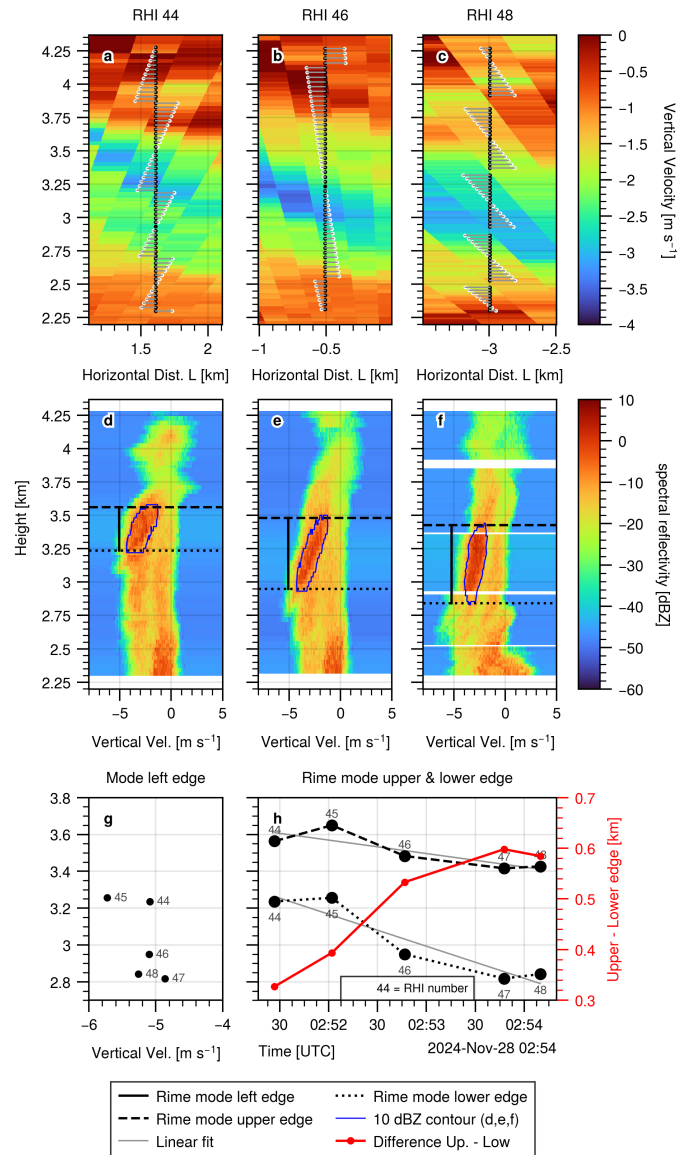


Figure 13. (a), (b), (c): Projection of range gates (white) onto vertical profiles (black) for the construction of spectral column vertical profiles (SCVP). A maximum horizontal projection distance of 200 m is allowed. (d), (e), (f): SCVP along the profiles in (a) to (c). The dashed, dotted and solid line depicts the upper, lower and left edge of the rime mode, respectively. (g): Height (similar to time) evolution of the left edge velocity of the rime mode. (h) Time evolution of the upper and lower edge of the rime mode. Grey lines show a linear regression to the data. The red line, with respect to the right axis, denotes the difference between the upper and lower edge height. One can see how the lower edge exhibits a faster downward motion and the rime mode is increasingly stretched out.



Recent studies by Frech et al. (2026) and Ockenfuß et al. (2026a) demonstrate that THI from operational C-band weather
435 radars can also detect riming. They present cases in which similar riming signatures appear simultaneously in multiple radars
separated by approximately 70 km, supporting a substantial spatial extent.

Ockenfuß et al. (2025) further estimated the long-term statistics of the spatial extent of riming by multiplying the duration
of riming signatures in THI with the background wind speed, yielding a median extent of 13 km. However, they noted that this
method relies on strong assumptions, namely consistent advection with the background wind and negligible intrinsic temporal
440 evolution, which they were not able to prove. They also point out that radar scans through intense riming events could provide
information on spatial structure, but for slanted viewing angles Doppler velocities are dominated by horizontal wind and are
therefore of limited use for riming detection.

Our results demonstrate that these challenges can be overcome. The cases we presented correspond conceptually to fall
streak scenarios of type B and type C in Figure 1. For these scenarios, the advection assumption holds, and multiplying the
445 duration in the THI (Figure 1e,h) by the wind speed provides a valid estimate of the horizontal size of the riming initiation
region (Figure 1d,g). In contrast, this approach would fail for scenario A: the long duration in Figure 1b would falsely suggest
a large seeding region, although the actual source is the localized cell shown in Figure 1a.

5.2 Assumptions and limitations when removing the horizontal wind contribution from Doppler observations

In general, retrieving the spatial velocity field from an RHI scan is underdetermined by a factor of two: each Doppler mea-
450 surement depends on two unknowns, namely the vertical velocity and the in-plane horizontal velocity component. Without
additional constraints, different realizations of the velocity field could therefore explain the same measurements.

To reduce this ambiguity, we assume a linear model for the horizontal wind component (Equation 12) and attribute the
remaining fluctuations to the vertical velocity. Although this assumption appears simplistic—since convergence, divergence,
and turbulence create variations in the horizontal wind—several arguments indicate that it performs very well for the presented
455 cases and that the spatial fields in Figure 7 and Figure 12 represent the actual vertical velocity field realistically.

First, as shown in Figure 3, within $\pm 45^\circ$ of the vertical the radar is more sensitive to variations in vertical velocity than in
horizontal velocity. Second, characteristic spectral features, such as multimodal structures and coherent vertical mode patterns
(Figure 8, Figure 9, Figure 13), coincide with regions of enhanced vertical velocity in the reconstructed fields. This strongly
suggests a microphysical origin of these patterns. If the observed signatures were caused by horizontal wind variability instead,
460 we would not expect the formation of multiple spectral peaks, because horizontal wind affects all particles equally and primarily
broadens the spectra.

Finally, the temporal evolution of the reconstructed fields provides further support. In Case 2, the bubble structure origi-
nates from enhanced negative Doppler velocities in the raw data, indicating motion toward the radar. While such a signal
could in principle also result from increased horizontal flow toward the radar, this scenario would imply a sign change in the
465 reconstructed field, as the horizontal perturbation advects across the radar location. First, we would expect decreased Doppler
velocity upstream, then increased Doppler velocity downstream. No such sign reversal is observed in Figure 12.



In addition to the general choice of the horizontal wind model $M_{\mathcal{P}}$, our method relies on another, more subtle premise. Even if we assume that the in-plane horizontal wind can be described by a linear model $M_{\mathcal{P}}$ (Equation 12), the system of equations remains weakly underdetermined. For example, for an RHI with 30 measurements per height level, we obtain 32 unknowns:
470 two parameters (γ_0 and λ) describing the horizontal wind and 30 vertical velocity components w_i .

By fitting $M_{\mathcal{P}}$ to the raw Doppler data using a least-squares approach, we implicitly favor the solution with minimal variance. That is, we attribute as much variability as possible to the horizontal wind model before assigning the remaining fluctuations to the vertical velocity. As a consequence, the reconstructed vertical velocity fields may appear slightly smoother than in reality.

We tested whether this effect influences the interpretation of Case 1, which exhibits pronounced horizontal homogeneity.
475 Replacing the two-parameter linear model with a one-parameter constant wind model yields an almost identical spatial reconstruction. The only exception is RHI scan No. 29, which shows strong downward motion in the outermost, most slanted beams (see Figure C1). As discussed in subsection 3.2.2, such a pattern typically indicates an uncorrected linear trend in the horizontal wind rather than persistent riming confined to the outermost beams. We therefore retained the linear model for the analysis in subsection 4.1.1.

480 6 Summary and recommendations for future observations

Currently, most radars and other ground based remote sensing devices operate in a vertically pointing mode, producing time-height images (THIs). As we have discussed in section 2, THIs show a combination of the spatial structure and time evolution of a system. In order to study particle evolution in THIs, we need to assume horizontal homogeneity. Conversely, in order to study the spatial organization of particles, we need information about the particle evolution, especially particle sedimentation
485 velocity. In this study, we investigated to which degree scans, specifically range-height indicator (RHI) scans, can help to assess the validity of these assumptions in THI analysis and even overcome the limitations of THI. A first step is the inclusion of sporadic RHI scans in a THI setup. As we have shown in subsection 4.1.2, the RHI provides an actual spatial view on the scene. If the system is sufficiently homogeneous, we know that we can safely study the particle evolution from THI, e.g. using classical fall streak tracking or spectral analysis like in subsection 4.1.3. Since for the analyzed case, we found constant
490 sedimentation velocity, we also demonstrated the converse analysis. In subsection 4.1.5, we assume constant sedimentation velocity and use backward trajectories to reconstruct the 3D spatial evolution of the scene using only vertical observations.

In subsection 4.2, we then show an example of a spatially inhomogeneous situation. As we demonstrate in subsection 4.2.1, a THI based process analysis based on fall streaks would lead to false conclusions in this case. A single RHI at the right time can save us from such a mistake, but it does not allow us to overcome the limitations. For that, we need a series of
495 multiple RHI scans, aligned with the wind direction. As shown in subsection 4.2.2, this allows for the lagrangian tracking of a specific group of particles even under inhomogeneous conditions. At first glance, performing continuous RHI scans seems like a trade off, since the "classical" THI perspective may be lost. However, this is not necessarily the case. By including a short stop at the vertical in each RHI scan, we obtain a vertical profile about every 40 s. As we show in subsection 4.1.3 and subsection 4.1.5, this is enough to apply the classical THI analysis methods, if the conditions for them are fulfilled.



500 This result suggests that THI might often be temporally oversampled with respect to the analysis methods applied to them. This is something that should be analyzed in future resolution experiments. However, recent results by Ockenfuß et al. (2026a) and Frech et al. (2026) point to a similar conclusion. Frech et al. (2026) showed that THI from operational weather radars, which record only one vertical profile every 5 min, can resolve many of the characteristic features of stratiform and convective systems. Ockenfuß et al. (2026a) compared that with continuous THI from cloud research radars, showing that algorithms
505 developed to process cloud radar data also work well on the coarser 5 min resolution.

Another common reason against the inclusion of RHI scans (or any scans) is that the Doppler velocity measurements are strongly influenced by the horizontal wind and that therefore Doppler velocity and Doppler spectra from scans are of limited use for microphysical analysis. As demonstrated, under the assumption of horizontally homogeneous horizontal wind, the methods introduced in section 3 allow for the reconstruction of Doppler moments and spectra from RHI scans. As shown in
510 subsection 4.1.3, it is possible to separate multiple peaks in the spectra until about 40° of zenith. With the newly introduced spectral column vertical profile (SCVP) technique, it is possible to lagrangianly track the Doppler spectra evolution of a single group of particles in space and time, as shown in subsection 4.2.4.

An interesting future application for the SCVP technique will be artificial seeding experiments, such as the recent CloudLab campaign (Henneberger et al., 2023). Since the seeding happens only localized, this represents a spatially inhomogeneous
515 situation. SCVP would potentially allow to reveal the Lagrangian evolution of the seeding signal in the Doppler spectra. Seeding campaigns are often conducted in stratiform, supercooled mixed-phase clouds similar to the riming example cases presented in this work. This suggests that the prerequisites for the SCVP method discussed in subsection 5.2 are likely fulfilled and our methods are applicable.

Another interesting application will be given by the combination of SCVP and polarimetry. Due to the azimuthally random
520 orientation of particles, continuous THI usually provide no useful polarimetric information. This changes with the inclusion of RHI scans. While this study focused on spectral reflectivity, the ability to track the lagrangian evolution of quantities like spectral differential reflectivity ($sZDR$), potentially in combination with artificial seeding, can provide novel insights in the growth of ice particles. This matches well with recent advances in lagrangian ice modeling (Brdar and Seifert, 2018) and the coupling of these models with polarimetric radar forward operators (von Terzi et al., 2026).

525 To extend our methodology to more turbulent or convective cases, some parameters may require adjustment. For instance, one might need to restrict the RHI elevation range to higher beams that are less sensitive to horizontal wind fluctuations. The optimal parameters can potentially be determined by combining a radar simulator with a large-eddy simulation (LES), similar to e.g. Oue et al. (2019). In addition, it is well known that multiple radars observing the same air volume from different viewing angles allow the retrieval of the full velocity vector (multi-Doppler radar wind retrieval; e.g., Potvin et al., 2012; North et al.,
530 2017). In such a configuration, the assumption of a horizontal wind model M_P becomes unnecessary. Even two radars would suffice if they perform overlapping RHI scans in the same plane. This setup would potentially allow for the calculation of SCVPs through convective cells and—if the cell track aligns with the RHI plane—to investigate the Lagrangian evolution of particle Doppler spectra within a convective storm.



535 Last, but not least, we want to point out that our methods are not restricted to radars. Other instruments like scanning lidars can benefit from the same approach. It is also worth mentioning that the upcoming 11th ESA Earth Explorer mission WIVERN (Illingworth et al., 2018) will involve scanning Doppler observations as well. Their approach to Doppler processing shows some similarities to our methods, for example the assumption of a linear model for the horizontal wind (European Space Agency, 2025).

540 *Code and data availability.* For the trajectory simulations in Figure 1 and Figure 10, we developed a general purpose Python advection simulator `advesi`. The package is freely available and open source at <https://github.com/Ockenfuss/advesi> (Ockenfuß, 2026a). Another open source Python package `windfit` provides methods to fit a constant or linear wind model to measured radial Doppler velocities, as presented in subsection 3.2. It is available at <https://github.com/Ockenfuss/windfit> (Ockenfuß, 2026b). The measurement data is available at <https://cloud.physik.lmu.de/index.php/s/S2GQYpebxctnRdg>. Note: This link is for review and will be replaced with a DOI before the final publication.

545 *Video supplement.* This publication is accompanied by four video supplements. "A_cell.mp4", "B_layer.mp4" and "C_localized.mp4" are animated versions of the three scenarios presented in Figure 1. "Backward_Trajectories.mp4" provides an animated version of Figure 10.

Appendix A: Peak and mode finder

550 The peak finder used for Doppler spectra peak detection in this work, for example in Figure 9, is based on the `FIND_PEA`KS function provided by SciPy (Virtanen et al., 2020). It operates on a 5 point averaged version of the original spectra. Peaks are detected based on a minimum peak height of -30dB, a minimum peak prominence of 5dB and a minimum peak distance of 3 samples (13.4 cm s^{-1} for vertically recorded spectra). For each peak, several properties like peak top, peak base, full MDV and limited MDV are calculated. The difference between full and limited MDV is explained in Figure A1. The peak finder operates on each range or height level independently. After peak detection, the peaks are clustered along the vertical into continuous "modes" using the mode finder algorithm. The modes are indicated by the marker colors in Figure 9. The mode finder starts 555 with the hightest spectrum, assigning each detected peak to a new mode. It then proceeds to the next spectrum below and searches for the two closest peaks in this spectrum and the higher spectrum. If the limited MDV of the closest peaks does not differ by more than 0.8 ms^{-1} , they get assigned to the same mode and are marked as handled. This step is repeated until there are no unhandled or sufficiently close peak pairs left. If there are still unnumbered peaks left in the lower spectrum, a new mode number is assigned to each of them. This process is repeated until the lowest spectrum at the bottom of a spectrogram is 560 processed.

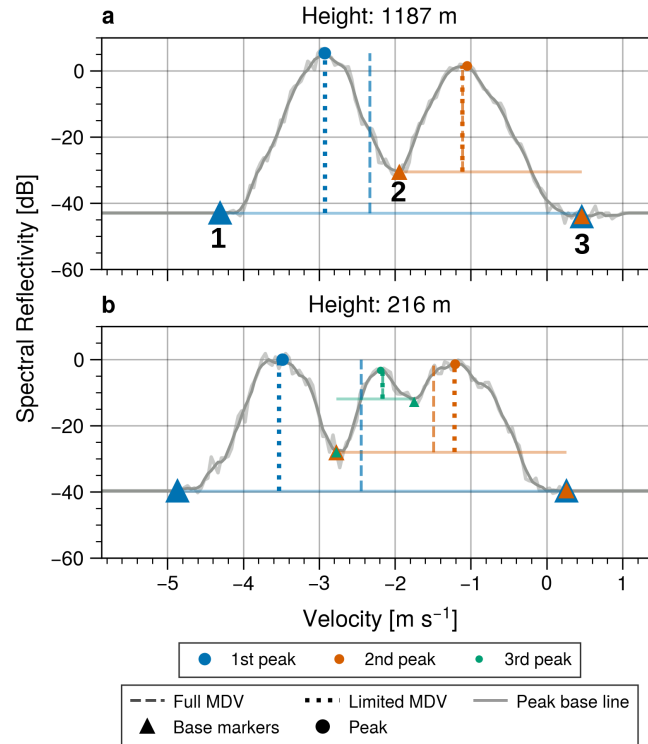


Figure A1. Example for Doppler spectra at two height levels. The peak finder algorithm operates on a smoothed version of the original spectrum. Both are shown in grey. Colors indicate the detected peaks. For each peak, we can see the peak top, peak bases and two versions of the peak mean Doppler velocity (MDV). The full MDV is calculated from left to right base of the corresponding peak. The limited Doppler velocity is calculated between the two bases, which are closest to the peak top, regardless of whether these bases belong to this peak or another peak in the spectra. For example, the full MDV of the first peak in (a) is calculated from base 1 to 3, while the limited MDV is calculated from base 1 to 2. Other moments of the spectrum can be calculated similarly in a full or limited version.

Appendix B: Optimal CVP beam separation level

Murphy et al. (2020) proposed using the intermediate elevation angle between two adjacent beams to define the separation level for projecting data from the lower and upper beams onto the CVP line. However, as illustrated in Figure B1a, this choice is not optimal with respect to projection distance. By placing the separation level slightly lower, as shown in Figure B1b, we avoid very long projections from the lower beam and instead use shorter projections from the upper beam. The optimal separation level follows directly from the geometry shown in Figure B2. We obtain the relations

$$Z_{1/2} = D \tan \theta_{1/2}, \quad h_{1/2} = d_{1/2} \tan \theta_{1/2}, \quad Z_s = Z_1 + h_1 = Z_2 - h_2. \quad (\text{B1})$$

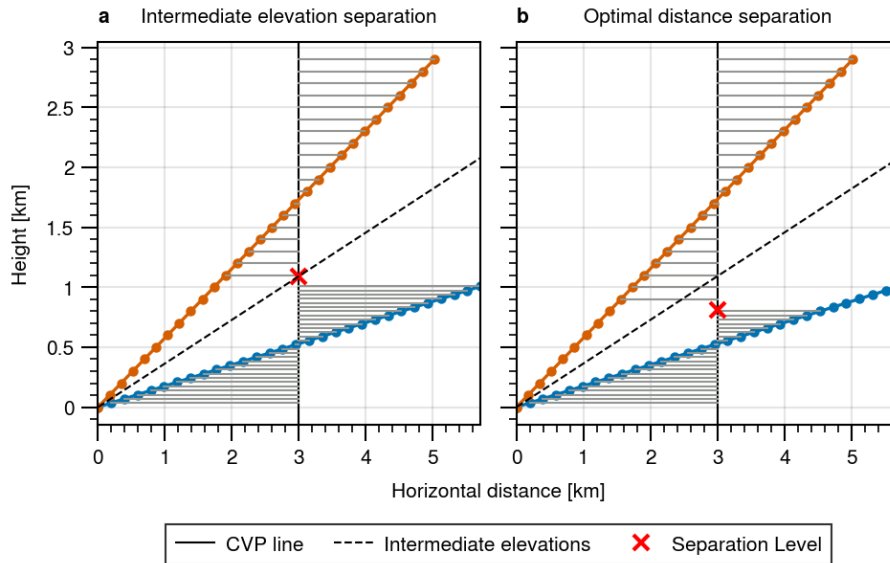


Figure B1. Illustration of two different choices for the beam separation level. **(a):** Separation based on the intermediate angle between the beams (Murphy et al., 2020). **(b):** This separation level minimizes the average projection distance of the original measurements to the vertical line.

Requiring equal projection distances, i.e., $d_1 = d_2$, yields a system of six equations for the six unknowns $Z_{1/2}$, $h_{1/2}$, Z_s , and d . Solving this system gives

$$570 \quad Z_s = 2D \frac{\tan \theta_1 \tan \theta_2}{\tan \theta_1 + \tan \theta_2}, \quad (\text{B2})$$

which defines the optimal separation height between two beams for given elevation angles and a CVP line located at distance D from the radar.

Appendix C: Case 1: RHI processing with constant wind model

575 Figure C1 shows the vertical velocity field, retrieved under the assumption of a horizontally constant horizontal wind (i.e. $\lambda = 0$ in Equation 12).

Appendix D: Surface weather charts for the example cases

Author contributions. PO developed the concept of this study, performed the measurements, analyzed the results and wrote the manuscript. GK and PO developed the Python framework to adaptively steer the scanning Ka-band radar. GK is also responsible for the general main-

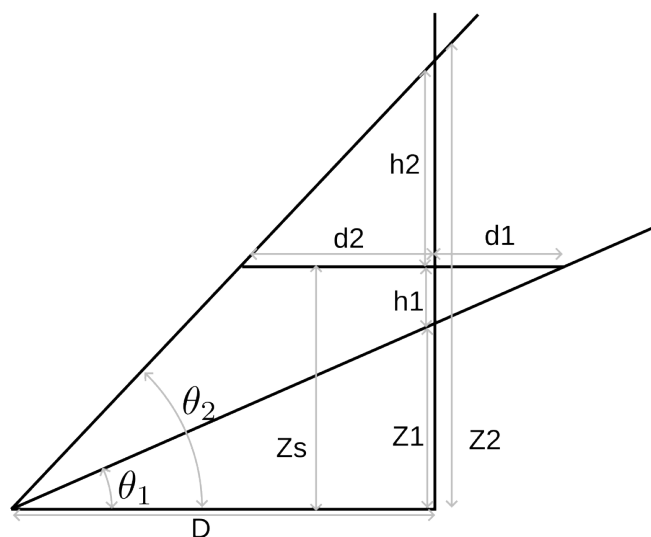


Figure B2. CVP geometry and definition of terms used in Equation B1.

580 tenance of the Ka-band radar. SK is responsible for the X-band radar operation and provided longterm radar experience to this study. IP performed the synoptic analysis of the presented cases.

Competing interests. In addition to her affiliation with the Munich Institute of Meteorology at LMU Munich, IP is employed by the German Meteorological Service (DWD).

585 *Acknowledgements.* This work has been supported by the DFG Priority Program SPP2115 “Fusion of Radar Polarimetry and Numerical Atmospheric Modelling Towards an Improved Understanding of Cloud and Precipitation Processes” (PROM) under Grant PROM-POMODORI (Project Number 408012686) and PROM-ICEPOLCKA (Project Number 408027579). We also acknowledge support for hardware upgrades and long-term operation of the two Doppler radars by ACTRIS-D (Grant number 01LK2001E), funded by the Federal Ministry of Education and Research (BMBF) under the FONa Strategy “Research for Sustainability.” In the production of this study, tools based on artificial intelligence (AI) were used. Specifically, “ChatGPT 5.4” by OpenAI and “Claude” by Anthropic assisted in simple, repetitive code generation tasks (plotting and formatting), as well as in improving the wording and formulation of this manuscript. All ideas and concepts are developed
590 without AI assistance exclusively by the authors.

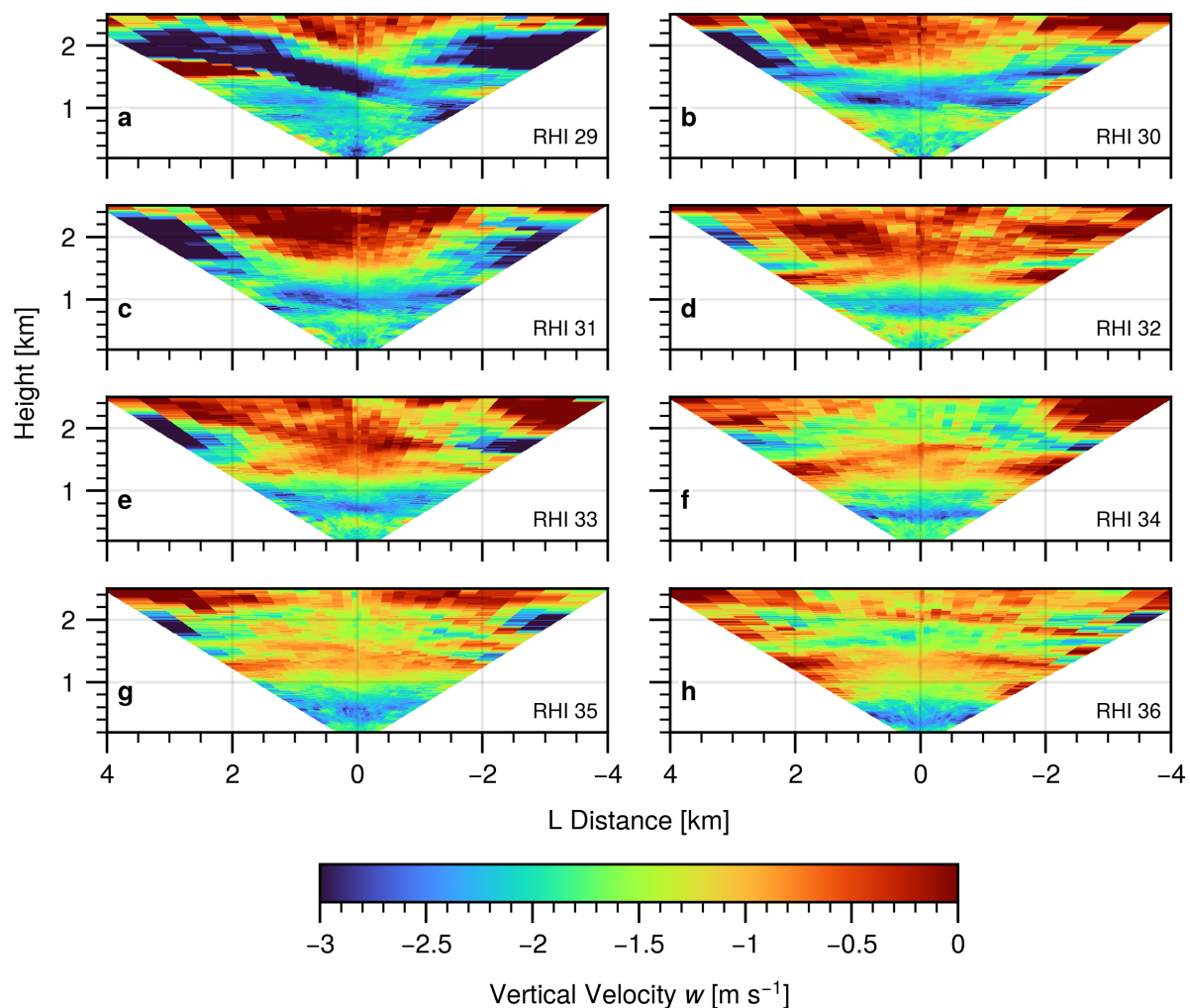


Figure C1. Spatial reconstruction of the vertical velocity field, as in Figure 7, but with the constant horizontal wind model (Equation 10) instead of the linear horizontal wind model.

References

- Icon D2 Forecast Germany, DWD Open Data Server, <https://opendata.dwd.de/weather/nwp/icon-d2/grib/>, accessed 10 November 2025. Description at https://dwd-geoportal.de/products/G_E6D/, 2024.
- Andrews, T., Gregory, J. M., Webb, M. J., and Taylor, K. E.: Forcing, feedbacks and climate sensitivity in CMIP5 coupled atmosphere-ocean climate models, *Geophysical Research Letters*, 39, <https://doi.org/10.1029/2012gl051607>, 2012.
- 595 Borque, P., Kollias, P., and Giangrande, S.: First Observations of Tracking Clouds Using Scanning ARM Cloud Radars, *Journal of Applied Meteorology and Climatology*, 53, 2732–2746, <https://doi.org/10.1175/jamc-d-13-0182.1>, 2014.

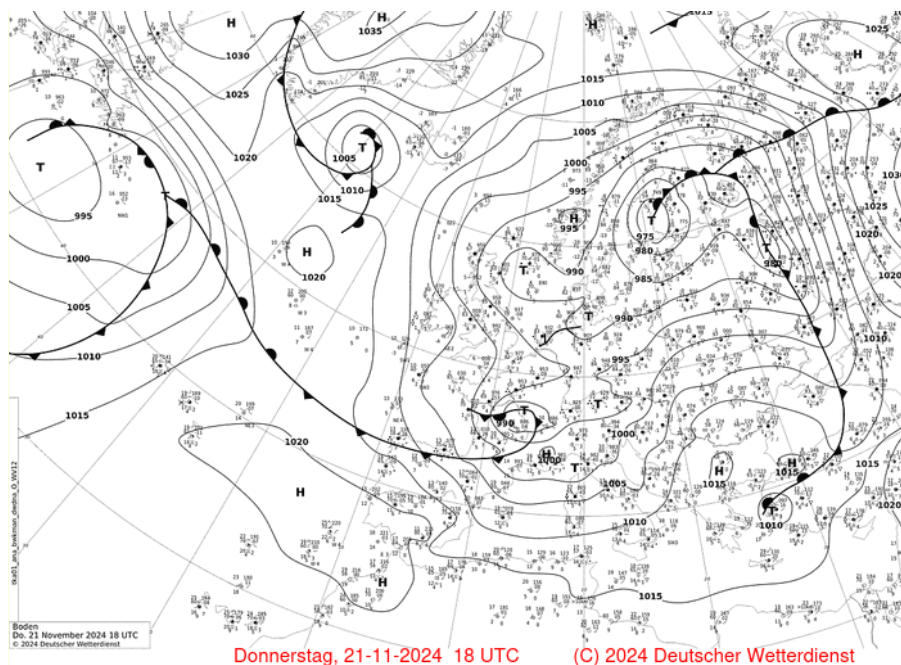


Figure D1. Surface analysis chart in the map section Europe - North Atlantic from 21 November 2024, 18 UTC. [From Wetter3]

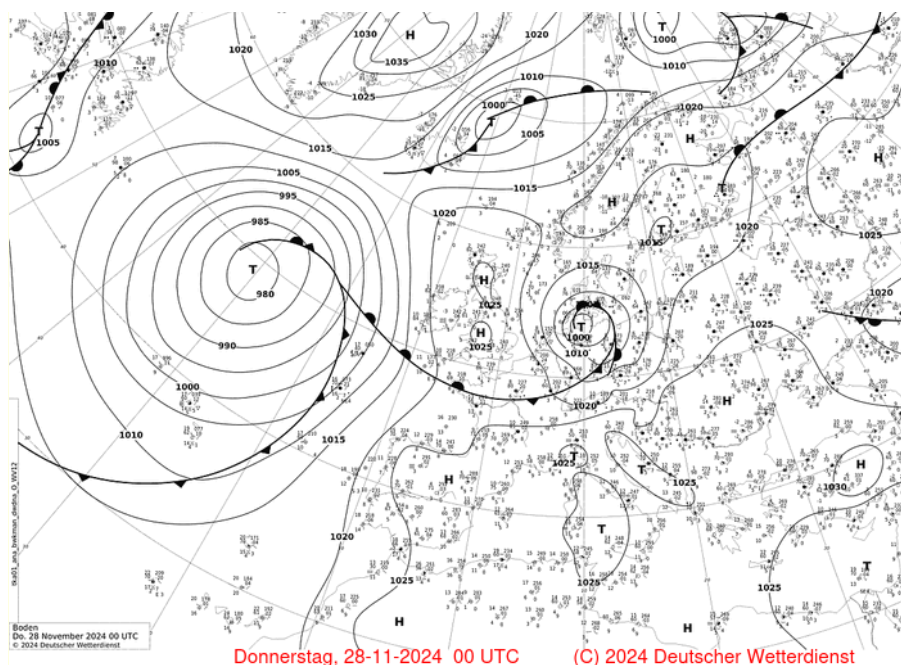


Figure D2. Surface analysis chart in the map section Europe - North Atlantic from 28 November 2024, 00 UTC. [From Wetter3]



- Borys, R. D., Lowenthal, D. H., and Mitchell, D. L.: The relationships among cloud microphysics, chemistry, and precipitation rate in cold mountain clouds, *Atmospheric Environment*, 34, 2593–2602, [https://doi.org/10.1016/s1352-2310\(99\)00492-6](https://doi.org/10.1016/s1352-2310(99)00492-6), 2000.
- 600 Borys, R. D., Lowenthal, D. H., Cohn, S. A., and Brown, W. O. J.: Mountaintop and radar measurements of anthropogenic aerosol effects on snow growth and snowfall rate, *Geophysical Research Letters*, 30, n/a–n/a, <https://doi.org/10.1029/2002gl016855>, 2003.
- Brdar, S. and Seifert, A.: McSnow: A Monte-Carlo Particle Model for Riming and Aggregation of Ice Particles in a Multidimensional Microphysical Phase Space, *Journal of Advances in Modeling Earth Systems*, 10, 187–206, <https://doi.org/10.1002/2017ms001167>, 2018.
- Browning, K. A. and Wexler, R.: The Determination of Kinematic Properties of a Wind Field Using Doppler Radar, *Journal of Applied Meteorology*, 7, 105–113, [https://doi.org/10.1175/1520-0450\(1968\)007<0105:tdokpo>2.0.co;2](https://doi.org/10.1175/1520-0450(1968)007<0105:tdokpo>2.0.co;2), 1968.
- 605 DeLaFrance, A., McMurdie, L. A., Rowe, A. K., and Conrick, R.: Effects of Riming on Ice-Phase Precipitation Growth and Transport Over an Orographic Barrier, *Journal of Advances in Modeling Earth Systems*, 16, <https://doi.org/10.1029/2023ms003778>, 2024.
- European Space Agency: Report for Mission Selection: Earth Explorer 11 Candidate Mission WIVERN, <https://doi.org/10.5281/ZENODO.15607041>, 2025.
- 610 Feingold, G., Glassmeier, F., Zhang, J., and Hoffmann, F.: Opinion: Inferring Process from Snapshots of Cloud Systems, <https://doi.org/10.5194/egusphere-2025-1869>, 2025.
- Frech, M., Kneifel, S., Ockenfuss, P., and Gergely, M.: Exploring the Untapped Potential of Operational Weather Radars for Vertical Profiling of Precipitation and Clouds, *Bulletin of the American Meteorological Society*, 107, E127–E141, <https://doi.org/10.1175/bams-d-24-0113.1>, 2026.
- 615 Gao, F. and Han, L.: Implementing the Nelder-Mead simplex algorithm with adaptive parameters, *Computational Optimization and Applications*, 51, 259–277, <https://doi.org/10.1007/s10589-010-9329-3>, 2010.
- Grabowski, W. W., Morrison, H., Shima, S.-I., Abade, G. C., Dziekan, P., and Pawlowska, H.: Modeling of Cloud Microphysics: Can We Do Better?, *Bulletin of the American Meteorological Society*, 100, 655–672, <https://doi.org/10.1175/bams-d-18-0005.1>, 2019.
- Görsdorf, U., Lehmann, V., Bauer-Pfundstein, M., Peters, G., Vavriv, D., Vinogradov, V., and Volkov, V.: A 35-GHz Polarimetric Doppler Radar for Long-Term Observations of Cloud Parameters—Description of System and Data Processing, *Journal of Atmospheric and Oceanic Technology*, 32, 675–690, <https://doi.org/10.1175/jtech-d-14-00066.1>, 2015.
- 620 Hajipour, M., Seifert, P., Griesche, H., Ohneiser, K., and Radenz, M.: Identification of multiple co-located hydrometeor types in Doppler spectra from scanning polarimetric cloud radar observations, *Atmospheric Measurement Techniques*, 18, 5199–5222, <https://doi.org/10.5194/amt-18-5199-2025>, 2025.
- 625 Henneberger, J., Ramelli, F., Spirig, R., Omanovic, N., Miller, A. J., Fuchs, C., Zhang, H., Bühl, J., Hervo, M., Kanji, Z. A., Ohneiser, K., Radenz, M., Rösch, M., Seifert, P., and Lohmann, U.: Seeding of Supercooled Low Stratus Clouds with a UAV to Study Microphysical Ice Processes: An Introduction to the CLOUDLAB Project, *Bulletin of the American Meteorological Society*, 104, E1962–E1979, <https://doi.org/10.1175/bams-d-22-0178.1>, 2023.
- Hersbach, H., Bell, B., Berrisford, P., Hirahara, S., Horányi, A., Muñoz-Sabater, J., Nicolas, J., Peubey, C., Radu, R., Schepers, D., Simmons, A., Soci, C., Abdalla, S., Abellan, X., Balsamo, G., Bechtold, P., Biavati, G., Bidlot, J., Bonavita, M., De Chiara, G., Dahlgren, P., Dee, D., Diamantakis, M., Dragani, R., Flemming, J., Forbes, R., Fuentes, M., Geer, A., Haimberger, L., Healy, S., Hogan, R. J., Hólm, E., Janisková, M., Keeley, S., Laloyaux, P., Lopez, P., Lupu, C., Radnoti, G., de Rosnay, P., Rozum, I., Vamborg, F., Villaume, S., and Thépaut, J.: The ERA5 global reanalysis, *Quarterly Journal of the Royal Meteorological Society*, 146, 1999–2049, <https://doi.org/10.1002/qj.3803>, 2020.



- 635 Heymsfield, A. J., Schmitt, C., Chen, C.-C.-J., Bansemer, A., Gettelman, A., Field, P. R., and Liu, C.: Contributions of the Liquid and Ice Phases to Global Surface Precipitation: Observations and Global Climate Modeling, *Journal of the Atmospheric Sciences*, 77, 2629–2648, <https://doi.org/10.1175/jas-d-19-0352.1>, 2020.
- Hogan, R. J. and Kew, S. F.: A 3D stochastic cloud model for investigating the radiative properties of inhomogeneous cirrus clouds, *Quarterly Journal of the Royal Meteorological Society*, 131, 2585–2608, <https://doi.org/10.1256/qj.04.144>, 2005.
- 640 Houze, R. A. and Medina, S.: Turbulence as a Mechanism for Orographic Precipitation Enhancement, *Journal of the Atmospheric Sciences*, 62, 3599–3623, <https://doi.org/https://doi.org/10.1175/JAS3555.1>, 2005.
- Illingworth, A. J., Battaglia, A., Bradford, J., Forsythe, M., Joe, P., Kollias, P., Lean, K., Lori, M., Mahfouf, J.-F., Melo, S., Midthassel, R., Munro, Y., Nicol, J., Potthast, R., Rennie, M., Stein, T. H. M., Tanelli, S., Tridon, F., Walden, C. J., and Wolde, M.: WIVERN: A New Satellite Concept to Provide Global In-Cloud Winds, Precipitation, and Cloud Properties, *Bulletin of the American Meteorological Society*, 99, 1669–1687, <https://doi.org/10.1175/bams-d-16-0047.1>, 2018.
- 645 Kalesse, H., Szyrmer, W., Kneifel, S., Kollias, P., and Luke, E.: Fingerprints of a riming event on cloud radar Doppler spectra: observations and modeling, *Atmospheric Chemistry and Physics*, 16, 2997–3012, <https://doi.org/10.5194/acp-16-2997-2016>, 2016.
- Kneifel, S. and Moisseev, D.: Long-Term Statistics of Riming in Nonconvective Clouds Derived from Ground-Based Doppler Cloud Radar Observations, *Journal of the Atmospheric Sciences*, 77, 3495–3508, <https://doi.org/10.1175/JAS-D-20-0007.1>, 2020.
- 650 Kollias, P., Bharadwaj, N., Widener, K., Jo, I., and Johnson, K.: Scanning ARM Cloud Radars. Part I: Operational Sampling Strategies, *Journal of Atmospheric and Oceanic Technology*, 31, 569–582, <https://doi.org/10.1175/jtech-d-13-00044.1>, 2014a.
- Kollias, P., Jo, I., Borque, P., Tatarevic, A., Lamer, K., Bharadwaj, N., Widener, K., Johnson, K., and Clothiaux, E. E.: Scanning ARM Cloud Radars. Part II: Data Quality Control and Processing, *Journal of Atmospheric and Oceanic Technology*, 31, 583–598, <https://doi.org/10.1175/jtech-d-13-00045.1>, 2014b.
- 655 Korolev, A., McFarquhar, G., Field, P. R., Franklin, C., Lawson, P., Wang, Z., Williams, E., Abel, S. J., Axisa, D., Borrmann, S., Crosier, J., Fugal, J., Krämer, M., Lohmann, U., Schlenzcek, O., Schnaiter, M., and Wendisch, M.: Mixed-Phase Clouds: Progress and Challenges, *Meteorological Monographs*, 58, 5.1–5.50, <https://doi.org/https://doi.org/10.1175/AMSMONOGRAPHIS-D-17-0001.1>, 2017.
- Kumjian, M. R., Prat, O. P., Reimel, K. J., van Lier-Walqui, M., and Morrison, H. C.: Dual-Polarization Radar Fingerprints of Precipitation Physics: A Review, *Remote Sensing*, 14, 3706, <https://doi.org/10.3390/rs14153706>, 2022.
- 660 Lim, J. and Hoffmann, F.: Life Cycle Evolution of Mixing in Shallow Cumulus Clouds, *Journal of Geophysical Research: Atmospheres*, 129, <https://doi.org/10.1029/2023jd040393>, 2024.
- Marshall, J. S.: Precipitation Trajectories and Patterns, *Journal of Atmospheric Sciences*, 10, 25–29, [https://doi.org/10.1175/1520-0469\(1953\)010<0025:PTAP>2.0.CO;2](https://doi.org/10.1175/1520-0469(1953)010<0025:PTAP>2.0.CO;2), 1953.
- Matejka, T. and Srivastava, R. C.: An Improved Version of the Extended Velocity-Azimuth Display Analysis of Single-
- 665 Doppler Radar Data, *Journal of Atmospheric and Oceanic Technology*, 8, 453–466, [https://doi.org/https://doi.org/10.1175/1520-0426\(1991\)008<0453:AIVOTE>2.0.CO;2](https://doi.org/https://doi.org/10.1175/1520-0426(1991)008<0453:AIVOTE>2.0.CO;2), 1991.
- Mitchell, D. L., Zhang, R., and Pitter, R. L.: Mass-Dimensional Relationships for Ice Particles and the Influence of Riming on Snowfall Rates, *Journal of Applied Meteorology*, 29, 153–163, [https://doi.org/10.1175/1520-0450\(1990\)029<0153:mdrfip>2.0.co;2](https://doi.org/10.1175/1520-0450(1990)029<0153:mdrfip>2.0.co;2), 1990.
- Morrison, H., van Lier-Walqui, M., Fridlind, A. M., Grabowski, W. W., Harrington, J. Y., Hoose, C., Korolev, A., Kumjian, M. R.,
- 670 Milbrandt, J. A., Pawlowska, H., Posselt, D. J., Prat, O. P., Reimel, K. J., Shima, S., van Diedenhoven, B., and Xue, L.: Confronting the Challenge of Modeling Cloud and Precipitation Microphysics, *Journal of Advances in Modeling Earth Systems*, 12, <https://doi.org/10.1029/2019ms001689>, 2020.



- Mróz, K., Battaglia, A., Kneifel, S., von Terzi, L., Karrer, M., and Ori, D.: Linking rain into ice microphysics across the melting layer in stratiform rain: a closure study, *Atmospheric Measurement Techniques*, 14, 511–529, <https://doi.org/10.5194/amt-14-511-2021>, 2021.
- 675 Murphy, A. M., Ryzhkov, A., and Zhang, P.: Columnar Vertical Profile (CVP) Methodology for Validating Polarimetric Radar Retrievals in Ice Using In Situ Aircraft Measurements, *Journal of Atmospheric and Oceanic Technology*, 37, 1623–1642, <https://doi.org/10.1175/jtech-d-20-0011.1>, 2020.
- North, K. W., Oue, M., Kollias, P., Giangrande, S. E., Collis, S. M., and Potvin, C. K.: Vertical air motion retrievals in deep convective clouds using the ARM scanning radar network in Oklahoma during MC3E, *Atmospheric Measurement Techniques*, 10, 2785–2806, <https://doi.org/10.5194/amt-10-2785-2017>, 2017.
- 680 Ockenfuß, P.: Ockenfuss/advesi: Advesi v.1.0.0, <https://doi.org/10.5281/zenodo.19682756>, 2026a.
- Ockenfuß, P.: Ockenfuss/windfit: Windfit v.0.1.0, <https://doi.org/10.5281/zenodo.19681776>, 2026b.
- Ockenfuß, P., Gergely, M., Frech, M., and Kneifel, S.: Spatial and Temporal Scales of Riming Events in Nonconvective Clouds Derived From Long-Term Cloud Radar Observations in Germany, *Journal of Geophysical Research: Atmospheres*, 130, <https://doi.org/10.1029/2024jd042180>, 2025.
- 685 Ockenfuß, P., Frech, M., Gergely, M., and Kneifel, S.: First nationwide analysis of riming using vertical observations from the operational German C-band radar network, *Atmospheric Measurement Techniques*, 19, 2125–2147, <https://doi.org/10.5194/amt-19-2125-2026>, 2026a.
- Ockenfuß, P., Köcher, G., Bauer-Pfundstein, M., and Kneifel, S.: A Novel Framework for Automatic Scanning Radar Pointing Calibration Using the Sun, <https://doi.org/10.5194/egusphere-2025-5690>, 2026b.
- 690 Oue, M., Kollias, P., Shapiro, A., Tatarevic, A., and Matsui, T.: Investigation of observational error sources in multi-Doppler-radar three-dimensional variational vertical air motion retrievals, *Atmospheric Measurement Techniques*, 12, 1999–2018, <https://doi.org/10.5194/amt-12-1999-2019>, 2019.
- Pfützenmaier, L., Dufournet, Y., Unal, C. M. H., and Russchenberg, H. W. J.: Retrieving Fall Streaks within Cloud Systems Using Doppler Radar, *Journal of Atmospheric and Oceanic Technology*, 34, 905–920, <https://doi.org/10.1175/jtech-d-16-0117.1>, 2017.
- 695 Potvin, C. K., Shapiro, A., and Xue, M.: Impact of a Vertical Vorticity Constraint in Variational Dual-Doppler Wind Analysis: Tests with Real and Simulated Supercell Data, *Journal of Atmospheric and Oceanic Technology*, 29, 32–49, <https://doi.org/10.1175/jtech-d-11-00019.1>, 2012.
- Seifert, A., Leinonen, J., Siewert, C., and Kneifel, S.: The Geometry of Rimed Aggregate Snowflakes: A Modeling Study, *Journal of Advances in Modeling Earth Systems*, 11, 712–731, <https://doi.org/https://doi.org/10.1029/2018MS001519>, 2019.
- 700 Shupe, M. D., Kollias, P., Matrosov, S. Y., and Schneider, T. L.: Deriving Mixed-Phase Cloud Properties from Doppler Radar Spectra, *Journal of Atmospheric and Oceanic Technology*, 21, 660–670, [https://doi.org/10.1175/1520-0426\(2004\)021<0660:dmcdfd>2.0.co;2](https://doi.org/10.1175/1520-0426(2004)021<0660:dmcdfd>2.0.co;2), 2004.
- Virtanen, P., Gommers, R., Oliphant, T. E., Haberland, M., Reddy, T., Cournapeau, D., Burovski, E., Peterson, P., Weckesser, W., Bright, J., van der Walt, S. J., Brett, M., Wilson, J., Millman, K. J., Mayorov, N., Nelson, A. R. J., Jones, E., Kern, R., Larson, E., Carey, C. J., Polat, İ., Feng, Y., Moore, E. W., VanderPlas, J., Laxalde, D., Perktold, J., Cimrman, R., Henriksen, I., Quintero, E. A., Harris, C. R., Archibald, A. M., Ribeiro, A. H., Pedregosa, F., van Mulbregt, P., and SciPy 1.0 Contributors: SciPy 1.0: Fundamental Algorithms for Scientific Computing in Python, *Nature Methods*, 17, 261–272, <https://doi.org/10.1038/s41592-019-0686-2>, 2020.
- Vogl, T., Maahn, M., Kneifel, S., Schimmel, W., Moisseev, D., and Kalesse-Los, H.: Using artificial neural networks to predict riming from Doppler cloud radar observations, *Atmospheric Measurement Techniques*, 15, 365–381, <https://doi.org/10.5194/amt-15-365-2022>, 2022.



710 von Terzi, L., Ori, D., and Kneifel, S.: A microwave scattering database of oriented ice and snow particles: supporting habit-dependent growth models and radar applications (McRadar 1.0.0), *Geoscientific Model Development*, 19, 887–910, <https://doi.org/10.5194/gmd-19-887-2026>, 2026.

Wetter3: Archive DWD Germany, https://www.wetter3.de/archiv_dwd_dt.html, accessed 4 December 2025.

715 Zhang, Y., Zheng, H., Zhang, L., Huang, Y., Liu, X., and Wu, Z.: Assessing the Effect of Riming on Snow Microphysics: The First Observational Study in East China, *Journal of Geophysical Research: Atmospheres*, 126, <https://doi.org/10.1029/2020jd033763>, 2021.

Zängl, G., Reinert, D., Rípodas, P., and Baldauf, M.: The ICON (ICOsahedral Non-hydrostatic) modelling framework of DWD and MPI-M: Description of the non-hydrostatic dynamical core, *Quarterly Journal of the Royal Meteorological Society*, 141, 563–579, <https://doi.org/10.1002/qj.2378>, 2014.